Assessment of Formulations for Numerical Solutions of Low Speed, Unsteady, Turbulent Flows over Bluff Bodies.

Theresa Lynn Campioli

Thesis submitted to the faculty of the Virginia Polytechnic Institute and State University
in partial fulfillment of the requirements for the degree of

Master of Science
In
Aerospace & Ocean Engineering Department

Approved by:

_____
Dr. Joseph Schetz

_____
Reece Neel

_____
Dr. Devenport

April 28, 2005
Blacksburg, VA

Keywords: Turbulence, Bluff Body, Low-Speed,
Unsteady, CFD

Assessment of Formulations for Numerical Solutions of Low Speed, Unsteady, Turbulent Flows over Bluff Bodies.

Theresa L. Campioli

ABSTRACT

Two algorithms commonly used for solving low-speed flow fields are evaluated using an unsteady turbulent flow formulation. The first algorithm is the method of artificial compressibility which solves the incompressible Navier-Stokes equations. The second is a preconditioned system for solving the compressible Navier-Stokes equations. Both algorithms have been implemented into GASP Version 4, which is the flow solver used in this investigation. Unsteady numerical simulations of unsteady, 2-D flow over square cylinders are performed with comparisons made to experimental data. Cases studied include both a single-cylinder and a three-cylinder configuration. Two turbulence models are also used in the computations, namely the Spalart-Allmaras model and the Wilcox k-ω (1998) model. The following output data was used for comparison: aerodynamic forces, mean pressure coefficient, Strouhal number, mean velocity magnitude and turbulence intensity. The main results can be summarized as follows. First, the predictions are more sensitive to the turbulence model choice than to the choice of algorithm. The Spalart-Allmaras model overall produced better results with both algorithms than the Wilcox k-ω model. Second, the artificial compressibility algorithm produced slightly more consistent results compared with experiment.

Acknowledgements

This work would not have been possible without the support and knowledge of my advisor Dr. Joseph Schetz. He always encouraged my best work and gave me the opportunity of pursuing higher education. Also, I would like to thank Dr. Reece Neel for his patience and guidance over the past few years. His advice has been more than helpful. The entire staff at AeroSoft Inc. has been enthusiastic and informative for which I am very thankful. Thank you for the use of your office, computers and time. I have enjoyed my time working with you all. Thanks to Dr. Devenport for serving on my committee. I would also like to thank AEDC (Arnold Engineering and Development Center) for their financial support in this effort.

On a personal note, I would like to thank my family for inspiration and encouragement. Mom, Dad, Mary, Jenn and Jason, thank you for always being there for me and for your advice. Your love, encouragement, advice and constant support have been large part of my success. I would like to thank all of my friends here in Blacksburg. Thanks to Dan for your support, your smile always brightens my day. Thanks to Cathy for being the best of friends, someone I could always lean on in good times and bad. You are an inspiration to me in all that you do. Thanks to my neighbors and friends, Tim, Carrie, Ben and Toni for their friendships and good food. Thanks to my weekly lunch gang, Sarah, Ariel, Ernie and Dan for the light hearted conversations, help with homework and much needed breaks from work.

Table of Contents

List of Figures

List of Tables

Nomenclature

Roman Symbols

C_D	Drag coefficient	
C_L	Lift coefficient	
C_P	Pressure coefficient	
C_v	Specific heat	
D	Side length of cylinders	[m]
k	Turbulent kinetic energy (or TKE)	[m^2/s^2]
M	Mach number	
n	frequency of vortex shedding	[Hz}
P	Static pressure	[Pa]
Pr	Prandtl number	
R	Gas constant	
Re	Reynolds number	
St	Strouhal number	
t	Time	[s]
T	Static Temperature	[K]
ti	Turbulence Intensity	[%]
U	Local velocity	[m/s]
V	Free stream velocity	[m/s]
u,v,w	Cartesian velocity components	[m/s]
x,y,z	Cartesian coordinates	[m]

Greek Symbols

β	Compressibility parameter	
ε	Turbulence dissipation rate	[m^2/s^2]
μ	Laminar (molecular) viscosity	[Ns/m^2]
μ_T	Turbulent (eddy) viscosity	[Ns/m^2]
ν	Kinematic viscosity	[m^2/s]
ν_T	Turbulent viscosity	[m^2/s]
ρ	Density	[kg/m^3]
τ	Shear stress	[N/m^2]
ω	Turbulent frequency	[m^3/s^3]
Ω	Mean vorticity	

Subscripts

∞	freestream condition

Superscripts

$\bar{}$	Time-averaged Values

Chapter 1: Introduction

1.1 Background

The latter half of the past century has been spent attempting to model turbulent flows computationally. The ability to solve and better understand these flows is becoming more apparent with the improvement of computers and modeling tools. Computational fluid dynamics (CFD) technologies have become a vital part of design and analysis in both research and commercial industries. CFD offers the ability to make a very detailed and thorough study of flow-fields and is capable of solving a broad range of flow problems from incompressible, low-speed, low-Reynolds number to compressible, high-speed, high-Reynolds number flows.

The concentration of this research involves two aspects of numerical research. The first is the current algorithms used in solving inviscid, incompressible flows. The second is the models or simulations used in solving turbulent flows. More interest has been shown by the scientific community in the evaluation of turbulence models than in low-speed algorithms because of the greater relevance to practical cases.

Turbulent, low-speed flows pose problems when solving the compressible Navier-Stokes equations. First, the turbulence length scales that are to be resolved by the numerical grid have a large variance in sizes. Second, the equations are highly non-linear in the convective terms, which lead to internal layers with time varying position. Finally, in order to satisfy the incompressibility constraint at all times, the equations must be coupled at each time step.

Historically, incompressible low-Reynolds number flows were solved by pressure-based algorithms[1]. This approach is characterized by a formulation in which the momentum equations are solved in sequence for velocity components while using an estimate for the pressure distribution. It decouples the set of non-linear, governing equations in which a pressure Poisson equation is formed from the momentum and continuity equations. The pressure distribution is improved in a separate step until a divergence-free velocity field is obtained. PISO[2] and SIMPLE[3] are some examples of algorithms that employ this approach. In more recent years, density-based[4] algorithms that employ time-marching techniques have grown in popularity. These algorithms solve for all the unknowns as a coupled system.

This research is concerned with the numerical simulation of turbulent, unsteady, low-speed flow using density-based algorithms implemented into the GASP Version 4 flow solver. GASP offers two methods for solving low-speed, turbulent flow: the method of artificial compressibility and a method that preconditions the Roe flux scheme. The method of artificial compressibility was introduced by Chorin[5]. This method is commonly used in industry and research for solving complex, incompressible low-speed flows. Artificial compressibility is also known as the pseudo-compressibility method. A pseudo-time derivative of pressure is added to the continuity equation along with a compressibility parameter, β. The addition of the artificial term couples pressure and velocity and makes the system of equations hyperbolic in time, which enables it to be time-marched. Once convergence (steady state) is achieved, the artificial time term vanishes. Artificial compressibility was originally developed for steady flow simulations, but it can be used for unsteady flows using a dual-time stepping procedure. The artificial

compressibility method is an algorithm used to solve the incompressible Navier-Stokes equations.

The second option for solving low-speed flows in GASP is a modified Roe flux scheme based on preconditioning of the compressible Navier-Stokes equations. The preconditioned Roe approach is a variable property, fully coupled method. Using the standard Roe flux scheme, solution accuracy and numerical stability begin to break down around Mach 0.05 and below. The preconditioned Roe flux scheme removes this numerical limit and allows flows that are considered incompressible to be simulated with accuracy and stability. The convergence is made independent of Mach number by alerting the acoustic speeds of the system such that the eigenvalues become the same order[6]. The modifications to the standard Roe flux scheme used here are based on the preconditioning matrix of Weiss and Smith[6]. The preconditioned flux differs from the standard flux in the acoustic corrections which are appended to the average flux. The preconditioned Roe flux can handle both low-speed and high-speed flows. It can be applied to steady and unsteady flows, as well as chemically reacting (variable density) flows. Specific details of both the artificial compressibility method and the preconditioned Roe method implemented in GASP can be found in Ref [7]. The preconditioned Roe algorithm also employs a dual-time stepping method that treats the flow at each physical time step as a steady-state problem in pseudo-time. The equations used in solving the above methods can be found in Chapter 3.

Solving turbulent flows can be done by either Large Eddy Simulation and Direct Numerical Simulation or Reynolds averaged Navier-Stokes (RANS) turbulence models. When performing CFD simulations in which the Reynolds Averaged Navier-Stokes

(RANS) equations are solved, the choice of turbulence model is critical, because it contains some of the largest uncertainties in modeling. There are a variety of turbulence models used in modern CFD analysis to help better simulate the actual physics of the problem. An ideal model should introduce the minimum amount of complexity while capturing the essence of the relevant physics[8].

In this report, the turbulence model approach was used. In a turbulence model, equations are solved for some mean quantity. In simulations, equations are solved for a time-dependent velocity field that represents the velocity field for one realization of the turbulent flow.

Two of the simulation methods being used today are Direct Numerical Simulation (DNS) and Large Eddy Simulation (LES). DNS solves the Navier-Stokes equations for $U(\mathbf{x},t)$ for one realization of the flow. In DNS all length scales and time scales must be resolved, which makes solving these flows extremely expensive (computational cost increases with Re^3) and requires a lot of time. The flows that can utilize DNS are extremely low Re flows ($Re < 6000$). Therefore, with a Re of 1.3×10^4, DNS cannot be used for this research.

The second simulation method is LES, which directly solves for the large three-dimensional unsteady turbulent motions. The small scales need to be accounted for so a model for the influence of the small sub-grid scale motions is incorporated. LES can be more accurate for flows with large-scale unsteadiness, separation and vortex shedding, such as flow over bluff bodies. LES cost is more than two orders of magnitude more expensive than a Reynolds stress model[9]. The cost of using LES is driven by the size of the grid needed to resolve the small scale motions. The number of grid points needed to

resolve turbulent boundary layers using LES scales on the order of the Reynolds number squared[10]. Therefore, the size of the discretized volumes must decrease and the overall number of grid points increases significantly over using a RANS model. LES was not used for this research but numerical results using LES will be discussed for reference purposes.

RANS models solve the governing equations for the mean velocity field and then some use models to solve for the unknown Reynolds stresses. The Reynolds stresses can be determined by the turbulent-viscosity hypothesis or from the Reynolds-stress transport equations[9]. Since an ideal model has yet to be found, two different "levels" of turbulence models are analyzed in this research. These include the one-equation Spalart-Allamaras[11] model and the two-equation Wilcox k-ω (1998)[8] model. These models were chosen because each has a different level of complexity, as well as computational efficiency. The models use additional transport equations to model the turbulent viscosity. The k-ω model is a two-equation model, which means there are two additional equations that solve for two turbulence quantities, k and ω. The Spalart-Allmaras model is a one-equation model with a single transport equation that solves for the turbulent viscosity. Spalart-Allmaras is simple and easy to implement and use.

These models are run with the two different low-speed algorithms, and the results are compared with each other and experimental data in order to determine how accurately the flow is described by each model.

1.2 Motivation

The problem of low-speed, unsteady, turbulent flow over a bluff body is of interest for both practical and scientific reasons. From a practical viewpoint, the problem

has application to a wide variety of cases including flow over buildings, cars and bridges. Investigating this flow helps, for example, civil engineers design for wind loadings on buildings or it can help in the design of cars by providing force data. It is also of interest from a scientific viewpoint since it involves large-scale unsteadiness, separated flows, recirculation and wake frequencies. By simulating these complex flow phenomena using CFD, an in depth understanding can be obtained.

Another reason for motivation is the uncertainty in CFD modeling. Bluff body flow is turbulent which is hard to predict and model numerically. By assessing the various methods available to evaluate flows over bluff bodies, knowledge can be gained on which method is most capable of predicting the flow behavior.

We consider both an isolated square cylinder and a vertical row of three horizontal square cylinders to widen the practical scope of our studies and to include mutual interference effects.

The Arnold Engineering and Development Center (AEDC) funded this research in order to validate the low-speed, turbulent, unsteady modeling capabilities of GASP.

1.3 Flow Field Descriptions

In order to provide a critical assessment of the two low-speed formulations and how they interact with the turbulence models considered, the problem of turbulent flow over a 2-D cylinder with a square cross-section has been selected. Two different configurations were used, a single-cylinder and a three-cylinder model. The flow around each configuration is described below.

1.3.1 Single-Cylinder Configurations

The first of two configurations to be discussed is uniform approach flow over a single square cylinder. The grid was created using Gridgen[12]. The grid is two-dimensional, which models an infinitely long square-cylinder placed in a confined flow. The model is 0.0254 m on a side. The structured grid, with approximately 60,000 cells, was clustered around the surface of the cylinder in order to capture the boundary layer effects. The far-field boundary extended 40+ diameters away from the square cylinder. Figure 1.1 shows the grid close to the square cylinder.

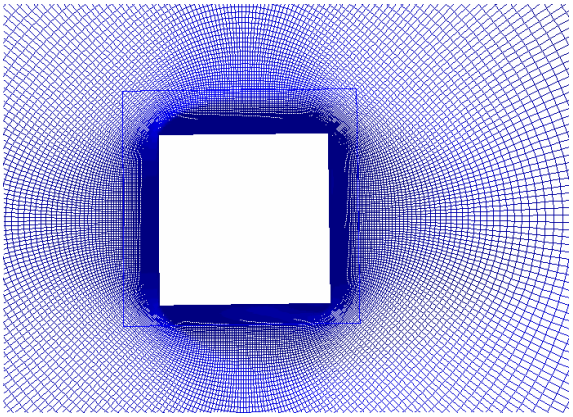

Figure 1.1 Up-close view of the single cylinder grid

The chosen boundary conditions will be discussed later. Some of the flow parameters are as follows:

- Free Stream Velocity: 7.65 m/s
- Density: 1.226 kg/m^2
- Inlet Mach number: 0.022
- Temperature: 297 K
- Turbulence intensity: 0.05

- Reynolds number (based on cylinder size): 1.3×10^4

The Reynolds number was selected to match experimental data. The single square cylinder results for pressure coefficient (Cp), Strouhal number (St), lift coefficient (C_L) and drag coefficient (C_D) are compared to experimental data from Lee[13] and Norberg[14], which will be discussed later.

The flow solver was run as 2nd order accurate in time with implicit, dual-time stepping. The time step was selected such that 120 cycles were performed per vortex shedding period (time step = 2×10^{-4}s).

A total of four simulations were run for this configuration. The artificial compressibility and preconditioned Roe algorithms were used for both the Spalart-Allmaras and the Wilcox k-ω turbulence models. The algorithms were run using 3rd order MUSCL[15] extrapolation spatial accuracy with no limiting.

1.3.2 Three-Cylinder Configuration

The second configuration is based on a turbulence generating experiment performed at Virginia Tech[16]. The experiment will be discussed further in Chapter 2. A schematic of the tunnel and three-cylinder configuration can be found in Figure 1.2 and Figure 1.3 shows a detailed view of the grid around the middle cylinder.

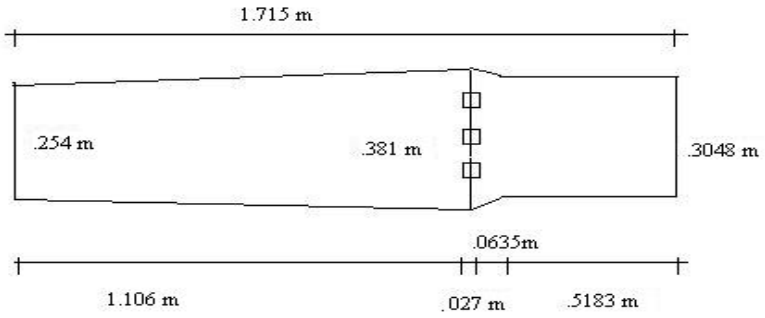

Figure 1.2 Schematic of three-cylinder configuration (side-view)

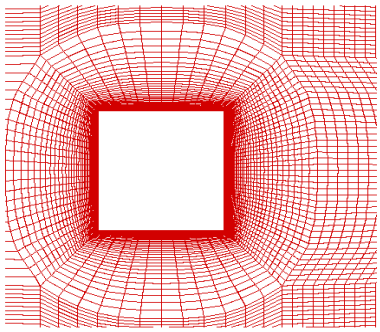

Figure 1.3 Detailed grid of middle cylinder (three-cylinder configuration).

The grid was created using Gridgen[12], and it mimicked the experimental wind tunnel setup. It was designed with three square cylinders, 0.0254 m in height (each bar). The cylinders were spaced vertically. Since the bars extended the width of tunnel in the experiment, a 2-D grid was used. The tunnel duct was 1.7158 m long and varied in height throughout. The duct at the inflow was 0.254 m high, and it expands to 0.381 m at the location of the square cylinders. Downstream of the cylinders, the tunnel contracts to 0.3048m tall at the test section. The grid had approximately 40,000 cells. The structured grid was clustered near the walls in order to capture the boundary layer development on

the cylinder surfaces and the top and bottom surfaces of the tunnel. The boundary conditions will be discussed later. Some of the key flow parameters are as follows:

- Free Stream Velocity: 20 m/s
- Density: 1.226 kg/m^2
- Inlet Mach number: 0.064
- Temperature: 297 K
- Turbulence intensity: 0.05
- Reynolds number (based on cylinder size): $2.7x10^4$

This case was run using the 1998 Wilcox k-ω turbulence model and artificial compressibility. The low-speed flux algorithm was then altered to preconditioned Roe and this case was run again. For comparison, the Spalart-Allmaras turbulence model was run for each of the low-speed flux algorithms. The algorithms were run using 3rd order MUSCL extrapolation[15] spatial accuracy with no limiting.

The flow solver was run as 2nd order accurate with implicit dual-time stepping. The time step was selected such that 380 cycles were performed per vortex shedding period (time step = 2×10^{-5} secs).

1.4 Overview of Thesis

This thesis begins with an introduction to the research of modeling low-speed, turbulent, unsteady flow over square cylinders. To accomplish this research, CFD was employed and the models and algorithms discussed are introduced in Chapter 1. The relevance for analyzing the numerical codes as well for using the square cylinder is also presented in this chapter. A past history of experimental and numerical work is presented

in Chapter 2, as well as a description of numerical approaches used in solving similar flows.

The governing equations used in this research can be found in Chapter 3, along with the equations of the artificial compressibility and preconditioned Roe algorithms as well as the Spalart-Allmaras and the Wilcox k-ω turbulence models.

The boundary conditions applied to each problem with any assumptions that may have been made are presented in Chapter 4. Also in Chapter 4 are the grid configurations for the single and three-cylinder formulations. The results of this research study are contained in Chapter 5. Conclusions and recommendations for future work can be found in Chapter 6, the last chapter. The bibliography and references finish the document.

Chapter 2: Review of Literature

Flow over bluff bodies has been a popular topic of research and has been studied both experimentally and numerically. This chapter will discuss previous experimental and computational research on low-speed flow over square cylinders. The experimental data presented in this chapter is used as a validation and verification tool for the numerical results of the research presented in this document. The numerical data reviewed is used as a reference tool. A brief description of the common methods of numerical simulation will also be discussed.

2.1 Experimental Data

This section discusses the experimental data used here for CFD validation. The first set of data discussed is by Lee[13] and Norberg[14] which was used to validate the single-cylinder configuration. Next, the experimental results of Nix[16] and Sayers[17] used to validate the three-cylinder configuration are presented.

2.1.1 Single-Cylinder Data

In 1975, B.E. Lee[13] studied the effects of turbulence on the surface pressure field of a square cylinder in low-speed flow at a Re of 1.7×10^4 based on the width. The focus of the paper was to vary the upstream turbulence and record the effects on pressure of the cylinder. Lee concluded that if the turbulence in the flow normal to the cylinder is increased, a rise in the mean pressure and consequently a reduction in mean drag were achieved. When the turbulence intensity is increased, the changes in the mean pressure distribution are influenced by changes in the behavior of the shear layers. The shear

layers reattach intermittently to the rear of the side faces and cause the vortex formation region to move downstream, thus raising the mean pressure. Lee also studied how the Strouhal number varied throughout the experiment. It was concluded that the St increases as the mean drag decreases. This is a result of the increase in frequency of vortex shedding by a smaller wake width and smaller vortex spacing. The current research utilizes the results of the pressure coefficient distribution and St on the cylinder with no upstream turbulence. The pressure distribution was recorded by 18 pressure taps on the surface of the cylinder. The pressure coefficient distribution can be found in Figure [2.1]. The mean C_P was measured from the center of the windward face, moving clockwise around the square cylinder. The St was found to be approximately 0.24.

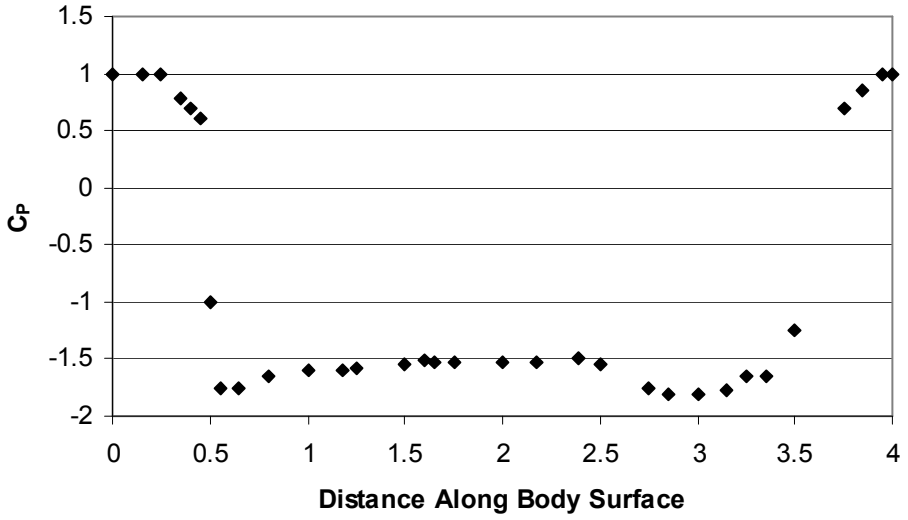

Figure 2.1 Pressure coefficient distribution on cylinder surface (Lee[13])

In 1993, C. Norberg[14] investigated the flow around and pressure forces on rectangular cylinders (for various angles of attack and aspect ratios) at a Re of 1.3×10^4 based on diameter. For validation here, only the data for zero angle of attack with an

aspect ratio of one square cylinder was used. The cylinder was exposed to a low-turbulence cross flow with a constant free stream velocity. Pressure taps on the cylinder surface were used to measure the pressure. Wake frequencies and associated Strouhal numbers were determined from hot wire measurements in the near-wake regions. The Strouhal number was calculated from the peak frequency in the power density spectrum. The square cylinders showed unstable vortex shedding in the experiment. Thus, when a CFD analysis is performed it should be run unsteady in order to capture the instabilities. The main results are summarized in Table 2.1.

Table 2.1 Experimental Results (Norberg[14])

Mean C_D	2.15
Mean C_L	0
St	0.1322

2.1.2 Three-Cylinder Data

A turbulence generating experiment was performed in a Virginia Tech wind tunnel by Drew Nix[16] in 2002. The purpose of this experiment was to create a desired amount of turbulence in the test section. The turbulence generating grid was comprised of three square cylinders that extended the width of the tunnel and were spaced vertically across the duct. Each square cylinder was 0.0254 m on a side. The spacing between the middle cylinder and the outer two cylinders was 1.0 diameter, 0.0254 m. The spacing between the outer cylinders and the walls was 2.5 diameters, 0.0635 m. The cylinders were placed 0.336 m upstream of the middle of the test section. Data was recorded in the test section at a location 0.5 m aft of the square-cylinder turbulence generating grid. A

picture of the turbulence generator and the upstream portion of the tunnel can be found in Figure [2.2]. The test section is not visible from the picture, but the segment of the wind tunnel that was modeled in the CFD analysis and the cylinders are shown.

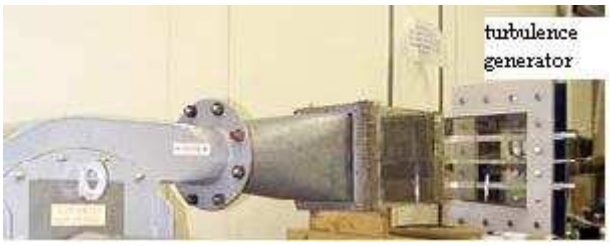

Figure 2.2 Picture of the turbulence generator (Nix[16]).

Using a Pitot probe and hot-wire anemometer to record data, the velocities and turbulence intensities were determined. The resultant data can be found in Figures [2.3] and [2.4]. The data in the figures represents the mean velocity magnitude and the turbulence intensity 0.5 m downstream of the cylinders. Two sets of data are shown for the tunnel without the turbulence generating grid and also for the tunnel with the grid. But, only the results with the grid are of interest in this study. The data was recorded between 0.0762 m (3 in) from the lower wall and 0.127 m (5 in) from the upper wall. The accuracy of the recorded data is questionable in that the velocity and turbulence intensity are fairly constant across the test section. For unsteady, highly turbulent, vortical flows, constant mean velocity and turbulence intensity are not expected.

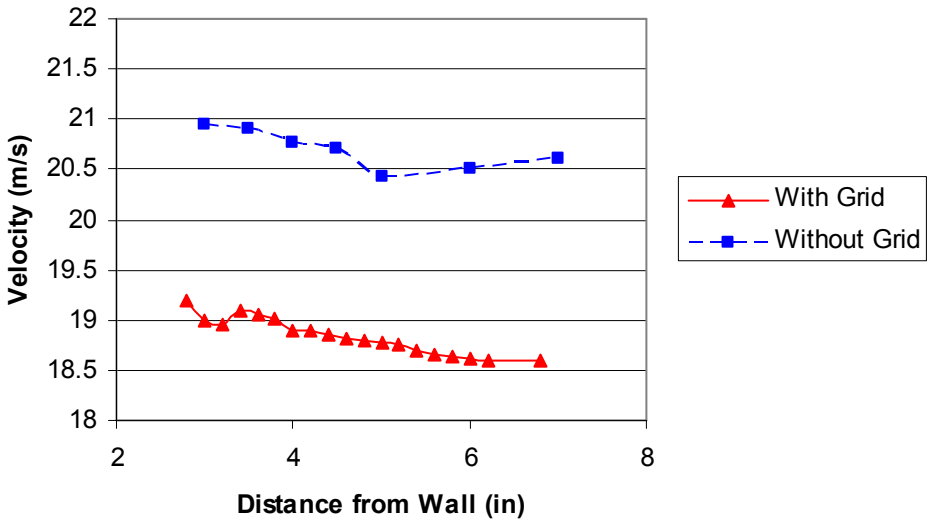

Figure 2.3 Vertical traverse mean velocity distribution 0.5 m downstream of grid (Nix[16]).

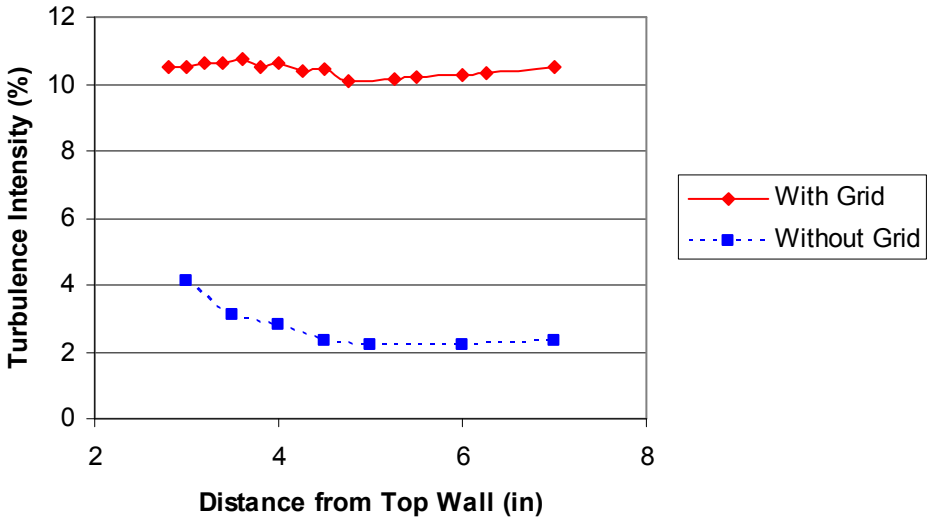

Figure 2.4Vertical traverse of the turbulence intensity 0.5 m downstream of grid (Nix[16]).

The turbulence generating experiment performed above did not investigate the forces, pressures and interactions of multiple cylinders. An experiment performed by Sayers[17] evaluated the effects of three cylinders placed transversely to and in line with the

flow at a Re of 3 x 10^4. The cylinders were 50 mm on a side. It was shown that when the cylinders were oriented transversely to the flow, the middle cylinder had a higher C_D than the outer cylinders. If the spacing between the cylinders was greater than 2 diameters, the drag on the middle cylinder was equal to the drag of a single cylinder under the same conditions. The pressures on the cylinders were also studied, and the results showed that when the spacing between cylinders was equal to the cylinder diameter, the pressure on the middle cylinder resembled a single cylinder test case. However, the pressure on the faces of the outer cylinders varied. The outer face (away from middle cylinder) had a much lower pressure than the face closest to the middle cylinder (gap side). The face pressures on the gap side resembled the pressures on the single cylinder test case.

2.2 Numerical Studies

The study of separated, unsteady, turbulent flows has been performed numerically for many decades. The flow over circular or square cylinders has been popular, because the simple geometry is easy to implement and the flow phenomena produced are of great interest to the scientific community. As the speed and power of computers have increased, more complex and sometimes more accurate methods have been used to simulate various flows. There will always be a trade-off between the complexity of numerical models and the speed and accuracy with which a solution will converge. In this section, previous computational studies of flow over square cylinders will be reviewed.

The majority of previous computational work emphasizes the choice of turbulence model, although there has been research on incompressible methods, such as that of Kwak et al[19] and Venkateswaran et al[20]. They showed that density-based algorithms were

more successful than pressure-based in solving incompressible flows. Also, Kwak states that the artificial compressibility method was his method of choice for solving low-speed flows. It was shown that the improved predictions of the preconditioning methods require more time-steps.

A turbulence model evaluation by Horstman et al. [21] compared the Wilcox model and two Reynolds Stress models to experimental data for compressible boundary layer flows with adverse pressure gradients. All models tested did an adequate job in predicting the experimental results. It was concluded that the Wilcox model is a sufficient model to use in adverse pressure gradients and in separation. According to Wilcox[22], the strongest feature of the k-ω model is the ease with which the equations can be integrated through the viscous sub-layer, which is in contrast to the k-ε model that is notoriously difficult to integrate through the sub-layer. Wilcox also reiterates that the k-ω model performs better in adverse pressure gradients than the k-ε model.

Many papers have been written that discussed the k-ε turbulence model or a LES simulation. The k-ε model has been shown to poorly predict separation and adverse pressure gradients (Rodi[23] and Lee[24]). However, for square cylinders the separation point is set by the geometry and not the adverse pressure gradient as with circular cylinders. According to Rodi[23], conventional *k-ε* turbulence models have failed in predicting unsteady turbulent flows around blunt bodies (not just adverse pressure gradients), unless careful modifications suited to the specific cases were made. Lee[24] compared several *k-ε* models and an LES simulation. LES over-predicted and *k-ε* under-predicted the experimental forces on the bluff body. The *k-ε* model predicted reattachment on the upper and lower sides of the square-cylinders that was not shown in either the experiment or the

LES simulation. Lee concluded that for flow over a cube, the standard k-ε model produced rather poor results, because the periodic motion was strongly under-predicted. The two-equation k-ε model was not investigated in this research, since it showed poor results in earlier related work.

LES does prove to be a good choice in modeling accuracy but requires significantly more time and power to run a simulation and is highly dependent on the number of grids points used. Rodi et al[23] provided results of an LES study at $Re = 2.2 \times 10^4$ that showed the Strouhal number appeared to be less sensitive to the parameters of the simulation, whereas the drag coefficient showed more dependence. Murakami et al.[25] focused on LES with several subgrid-scale models on a three-dimensional square cylinder at $Re = 2.2 \times 10^4$. Also, 2D and 3D simulations were compared with experimental results, and the 2D simulations had large discrepancies most likely due to a lack of 3D vertical modeling in the wake.

Lo et al. [10] performed a computational study using a Detached Eddy Simulation, DES, in combination with Spalart-Allmaras modeling of flow over square and circular cylinders. A Reynolds-averaged approach was taken in the near-wall region and transitions to LES far from the wall. It was found that the straight LES simulation requires the number of grid points to be on the order of Re^2. It was shown that the DES/S-A case predicted slightly higher Strouhal numbers and lower recirculation lengths than experimental results. The streamwise velocity and pressure coefficient distribution compared well with experimental results.

Low-speed flows around bluff bodies produce certain phenomena that have been studied in previous research. An LES study performed in 2001 by Krajnovic et al.[26] at a

Re of 4 x 10^4 showed that a 3D surface mounted cube had reattachment on the top, back and lateral surfaces. The LES study also showed that a horseshoe vortex formed in front of the cube and created a low pressure region with lateral shedding. A second vortex was formed behind the cube, which produced two recirculation regions. Krajnovic had an interesting observation that the axes of the vortices behind the cube were tilted with respect to the vertical axes. This caused the vortices to interact in the symmetry plane. Another study of square-cylinders performed by Taylor et al.[27] showed that alternate vortex shedding gave rise to a vortex street. Taylor also showed that the time histories of lift and drag began impulsively but after a short period of time, settled down and eventually reached a fairly regular oscillatory cycle. Lastly, Taylor attributed the discrepancies in the 2D results to a lack of modeling of the 3D effects in the wake, such as the development of the streamwise component of vorticity due to the vortex stretching and roll-up of the span-wise vortices. Tamura et al. [27] studied the differences in 2D and 3D modeling. It was found that there were significant differences from 3D and 2D especially in the near wake region. The 3D structures gradually emerge by vortex instability; this was not predicted with the 2D model.

There have been few studies of square cylinders that evaluate the low-speed algorithms or that evaluate the two turbulence models in this research. Therefore, this research intends to provide insight beyond previous research on the applicability of the chosen methods for low-speed flow over square cylinders.

Chapter 3: Governing Equations and Software

This chapter will discuss the equations used in numerical simulations of fluid flows. These equations include the compressible and incompressible forms of the governing Navier-Stokes equations and how they are manipulated into more useful forms. The equations that comprise the two low-speed algorithms and two turbulence models of interest will be discussed. The commercial numerical solver used in this research was AeroSoft's General Aerodynamics Simulation Program (GASP). A brief description of the features of GASP is provided below.

3.1 GASP

The GASP Version 4 flow solver is a time-dependent, three-dimensional Reynolds averaged Navier-Stokes (RANS) solver. It solves the integral form of the governing equations using an upwind-based, finite-volume formulation. The solver is also capable of solving subsets of RANS which include thin-layer Navier-Stokes, parabolized Navier-Stokes (PNS), the Euler equations and the incompressible Navier-Stokes equations.

GASP supports multi-block, structured grid topologies. Steady state solutions are marched in time using local time stepping, while time-accurate flows are solved using a dual-time stepping procedure. The dual-time stepping method incorporates a second temporal derivative for converging the root of the time-accurate discretization. This makes the dual-time step method appropriate for use with the artificial compressibility

and preconditioned Roe algorithms, since both require time-stepping with non-physical time steps, which can destroy temporal accuracy when implemented in traditional time-dependent formulations.

An advantage of using the dual-time stepping method is that it has no stability restrictions concerning the time step. So, large physical time steps can be chosen so long as the steady-state solution in pseudo-time is converged, which does have a stability restriction on the pseudo-time step. For the time-accurate simulations presented here, the Newton sub-iteration scheme was used, which is a subset of the dual-time stepping procedure. For Newton sub-iterations, the pseudo-time step is set to infinity, and the physical time step is then adjusted to insure stability.

There are many choices for low-speed fluxes within GASP, but this study analyzes the two fluxes that can be applied to low-speed flows, artificial compressibility and preconditioned Roe. The turbulence models used in this research found in GASP are the one-equation Spalart-Allmaras model and the Wilcox two-equation model based on k-ω.

3.2 Governing Equations

This section will introduce the compressible Navier-Stokes equations and then modify the equations into a vector and an integral form. GASP employs a time averaging technique (Reynolds averaging) to the integral form of the Navier-Stokes equations, which will also be discussed in this section. Lastly, the inviscid form of the Navier-Stokes equations will be introduced.

3.2.1 Compressible Navier-Stokes Equations

The governing equations used in computational fluid dynamics are the Navier-Stokes equations. Without assumptions, they apply to Newtonian fluids, compressible, viscous, unsteady and heat-conducting flows. The Navier-Stokes equations consist of the continuity equation, the momentum equation and the energy equation. The continuity equation is the conservation of mass, the momentum equation is Newton's second law of motion and the energy equation is the first law of thermodynamics. These equations are generally in the form of:

Continuity Equation:

$$\frac{\partial \rho}{\partial t} + \frac{\partial (\rho U_i)}{\partial x_i} = 0 \qquad \textbf{3.1}$$

Momentum Equation:

$$\frac{\partial (\rho U_i)}{\partial t} + \frac{\partial}{\partial x}(\rho U_i U_j - \tau_{ij}) = -\frac{\partial P}{\partial x_i} \qquad \textbf{3.2}$$

Energy Equation:

$$\frac{\partial}{\partial t}[\rho E_t] + \frac{\partial}{\partial x_j}[\rho U_j (h + \frac{1}{2} U_i U_i)] = \frac{\partial}{\partial x_j}(U_i \tau_{ij}) - \frac{\partial q_j}{\partial x_j} \qquad \textbf{3.3}$$

Where

$$E_t = (e + \frac{1}{2} U_i U_i) \qquad \textbf{3.4}$$

$$\tau_{ij} = \mu[(\frac{\partial U_i}{\partial x_j} + \frac{\partial U_j}{\partial x_i}) - \frac{2}{3}\frac{\partial U_k}{\partial x_k}\delta_{ij}] \qquad \textbf{3.5}$$

$$q_j = -k\frac{\partial T}{\partial x_j} \qquad \textbf{3.6}$$

The term U_i is a vector representing the three velocity components. The term τ_{ij} is the viscous stress tensor. The Kronecker delta, δ_{ij}, takes the value of one if i=j and zero if i≠j.

The momentum equation is comprised of three equations; one in each spatial direction. Therefore, there are five equations. There are more unknowns than there are equations; as a result, it is necessary to add an additional equation to close the system. The additional equation is usually an equation of state that relates the thermodynamic variables (p,ρ,T, e,h). If e and ρ are assumed to be the independent variables then we have the relations:

$$p = p(e, \rho) \qquad \text{and} \qquad T = T(e, \rho) \tag{3.7}$$

If a thermally perfect gas is assumed then the perfect gas equation of state can be used for the first relation,

$$p = \rho R T \tag{3.8}$$

where R is the gas constant. If the gas is calorically perfect, a perfect gas with constant specific heats, we can use the linear relation:

$$e = c_v T \tag{3.9}$$

For fluids that are not calorically perfect, the coefficients of viscosity and thermal conductivity can be related using kinetic theory[18].

3.2.2 Vector Form of the Compressible Navier-Stokes Equations

GASP solves the integral, vector form of the RANS equations; the vector form will be discussed here. The continuity equation, three momentum equations and the energy equation are combined into a vector equation with vectors **U, E, F, G** and **J**. The vector **U** is a column vector of the conserved variables, the vectors **E, F** and **G** are column vectors which contain the flux terms and **J** is the source term vector. The vector

form of the compressible Navier-Stokes equations in Cartesian coordinates without body forces or external heat addition can be written as:

$$\frac{\partial \vec{U}}{\partial t}+\frac{\partial \vec{E}}{\partial x}+\frac{\partial \vec{F}}{\partial y}+\frac{\partial \vec{G}}{\partial z}=\vec{J} \qquad \textbf{3.10}$$

Equation [3.10] can be simplified by separating the terms **E, F** and **G** into the viscous fluxes and inviscid fluxes. Equation [3.10] now becomes:

$$\frac{\partial \vec{U}}{\partial t}+\left(\frac{\partial \vec{E}}{\partial x}+\frac{\partial \vec{F}}{\partial y}+\frac{\partial \vec{G}}{\partial z}\right)=\left(\frac{\partial \vec{E}_v}{\partial x}+\frac{\partial \vec{F}_v}{\partial y}+\frac{\partial \vec{G}_v}{\partial z}\right)+\vec{J} \qquad \textbf{3.11}$$

The **U** vector contains the following variables:

$$\vec{U}=\begin{bmatrix}\rho\\ \rho u\\ \rho v\\ \rho w\\ \rho E_t\end{bmatrix} \qquad \textbf{3.12}$$

The inviscid flux vectors, **E, F** and **G**, are:

$$\vec{E} = \begin{bmatrix} \rho u \\ \rho u^2 + p \\ \rho uv \\ \rho uw \\ (E_t + p)u \end{bmatrix}$$

$$\vec{F} = \begin{bmatrix} \rho v \\ \rho uv \\ \rho v^2 + p \\ \rho vw \\ (E_t + p)v \end{bmatrix}$$

$$\vec{G} = \begin{bmatrix} \rho w \\ \rho uw \\ \rho vw \\ \rho w^2 + p \\ (E_t + p)w \end{bmatrix} \qquad \textbf{3.13}$$

The viscous flux vectors, $\mathbf{E_v}$, $\mathbf{F_v}$ and $\mathbf{G_v}$, are:

$$\vec{E}_v = \begin{bmatrix} 0 \\ \tau_{xx} \\ \tau_{xy} \\ \tau_{xz} \\ u\tau_{xx} + v\tau_{xy} + w\tau_{xz} - q_x \end{bmatrix}$$

$$\vec{F}_v = \begin{bmatrix} 0 \\ \tau_{xy} \\ \tau_{yy} \\ \tau_{yz} \\ u\tau_{xy} + v\tau_{yy} + w\tau_{yz} - q_y \end{bmatrix}$$

$$\vec{G}_v = \begin{bmatrix} 0 \\ \tau_{xz} \\ \tau_{yz} \\ \tau_{zz} \\ u\tau_{xz} + v\tau_{yz} + w\tau_{zz} - q_z \end{bmatrix} \qquad \textbf{3.14}$$

The inviscid fluxes, **E, F** and **G**, and the viscous fluxes, $\mathbf{E_v}$, $\mathbf{F_v}$ and $\mathbf{G_v}$, can be combined into matrices, $\mathbf{F}(\mathbf{U})$ and $\mathbf{F}_v(\mathbf{U})$. Simplifying equation [3.11], the vector form of the compressible Navier-Stokes equations can be obtained.

$$\frac{\partial \vec{U}}{\partial t} + \nabla \vec{F}(\vec{U}) - \nabla \vec{F}_v(\vec{U}) = \vec{J} \qquad \textbf{3.15}$$

3.2.3 Integral Form of the Compressible Navier-Stokes Equations

The integral form is obtained by integrating Equation 3.15 over the volume.

$$\iiint \left(\frac{\partial \vec{U}}{\partial t} + \nabla \vec{F}(\vec{U}) - \nabla \vec{F}_v(\vec{U}) \right) dV = \iiint \vec{J} dV \qquad \textbf{3.16}$$

Gauss' theorem, equation [3.17], is used to simplify the integral by transforming the volume integral into a surface integral.

$$\iiint \nabla \vec{F} dV = \iint \vec{F} \cdot \vec{n} dS \qquad \textbf{3.17}$$

Applying equation [3.17] to equation [3.16], the integral form of the (vector) Navier-Stokes equation can be obtained:

$$\frac{\partial}{\partial t} \iiint \vec{U} dV + \iint \left(\vec{F}(\vec{U}) - \vec{F}_v(\vec{U}) \right) \cdot \vec{n} dA = \iiint \vec{J} dV \qquad \textbf{3.18}$$

3.2.4 Reynolds-Averaged Navier-Stokes Equations

GASP solves the Reynolds averaged (RANS) or time-averaged Navier-Stokes. The RANS equations are derived by decomposing the dependent variables into time-mean and fluctuating components. This is called Reynolds decomposition. For example, the following equation time averages the u component of velocity,

$$u = \overline{U} + u' \tag{3.19}$$

where $\overline{U}$ is the Reynolds averaged or mean velocity and u' is the fluctuating component about that average; $\overline{U}$ is obtained from the following:

$$\overline{U} \equiv \int_{t_o}^{t_o+\Delta t} u dt \tag{3.20}$$

Note: the time-average of the fluctuating term, $\overline{u}'$ is defined to be zero.

Decomposing the Navier-Stokes equations and applying the note from above, equations [3.1, 3.2 and 3.3] become:

$$\frac{\partial \rho}{\partial t} + \frac{\partial}{\partial x_i}\left(\rho u_j\right) = 0$$

$$\frac{\partial}{\partial t}\left(\rho u_i\right) + \frac{\partial}{\partial x_j}\left(\rho u_i u_j\right) = -\frac{\partial \overline{p}}{\partial x_i} + \frac{\partial}{\partial x_j}\left(\tau_{ij} - \rho\overline{u'_i\, u'_j}\right)$$

$$\frac{\partial}{\partial t}\left(\rho c_p T\right) + \frac{\partial}{\partial x_j}\left(\rho c_p T u_j\right) = \frac{\partial p}{\partial t} + u_j \frac{\partial p}{\partial x_j} + \overline{u''_j \frac{\partial p}{\partial x_j}} + \frac{\partial}{\partial x_j}\left(k\frac{\partial T}{\partial x_j} + k\frac{\partial T''}{\partial x_j} - c_p\overline{\rho T'' u''_j}\right) + \overline{\Phi} \tag{3.21}$$

Where:

$$\tau_{ij} = \mu\left(\frac{\partial u_i}{\partial x_j} + \frac{\partial u_j}{\partial x_i}\right) \tag{3.22}$$

$$\overline{\Phi} = \overline{\tau_{ij}\frac{\partial u_i}{\partial x_j}} \tag{3.23}$$

Note: the over-bar has been dropped and it is now assumed that the terms are time averaged.

Time averaging the equations of motion creates new terms that need to be modeled. Looking at the Reynolds momentum equations, the new terms to be modeled are the turbulent stresses, $-\overline{\rho u'_i\, u'_j}$. This is called the Reynolds stress tensor and has six components, six more unknowns. The Reynolds stress tensor contains all of the influence

of turbulence but the fluctuating velocity components are unknown and a simple method does not exist to solve for them. In an attempt to complete the system of equations, turbulence models have been created to replace the Reynolds stress terms with a model of the mean-flow variables. This is the basis for turbulence modeling.

3.2.5 Inviscid, Incompressible Navier-Stokes Equations

The inviscid fluxes of the flow-field can be solved independently of the viscous fluxes. This is useful because the inviscid fluxes are less complex and they require less computing time to solve. The equations can be obtained by ignoring the viscous and the heat-transfer terms from the compressible Navier-Stokes equations. These equations are called the Euler equations or the inviscid, incompressible Navier-Stokes equations.

The continuity equation does not contain either viscous or heat transfer terms. If the flow is steady, than density can be factored out but otherwise there is no time dependency in the continuity equation for inviscid flows. The inviscid momentum equation was first derived by Euler in 1755. When the viscous terms are dropped equation [3.2] becomes

$$\rho \frac{D\overline{V}}{Dt} = \rho\vec{f} - \nabla p \qquad \textbf{3.24}$$

and equation [3.3], the energy equation, becomes

$$\rho \frac{De}{Dt} + p\left(\nabla \cdot \vec{V}\right) = 0 \qquad \textbf{3.25}$$

Similarly to the (viscous) Navier-Stokes equations, the Euler equations can be combined into vectors and integrated. The **F(U)** matrix below is comprised of the vectors from

equation [3.13] and the **U** and **J** vectors are the same as the Navier-Stokes equations. This produces the integral form of the incompressible Navier-Stokes equations:

$$\frac{\partial}{\partial t}\iiint \vec{U} dV + \iint \left(F(\vec{U}) \cdot \hat{n}\right) dA = \iiint J dV \qquad \textbf{3.26}$$

3.3 Low-Speed Inviscid Algorithms

The two available algorithms in GASP suitable for low-speed flow are the artificial compressibility algorithm and the preconditioned Roe algorithm. The equations that comprise both algorithms can be found in this section.

3.3.1 Artificial Compressibility

The artificial compressibility method was first introduced by Chorin[3] for use in obtaining steady-state solutions to the incompressible Navier-Stokes equations. The method of artificial compressibility has since evolved to handle time-accurate flows. Artificial compressibility solves constant density flows, which causes the time derivative term in the continuity equation to go to zero and the energy equation to uncouple from the momentum and continuity equations.

The original continuity equation is modified by adding an artificial time derivative of pressure representing the artificial compressibility. The new term couples the pressure and velocity.

$$\frac{\partial p}{\partial t} + \beta^2 \left(\frac{\partial u}{\partial x} + \frac{\partial v}{\partial y} + \frac{\partial w}{\partial z} \right) = 0 \qquad \textbf{3.27}$$

The governing equations are now hyperbolic and can be solved in a manner similar to the compressible equations. For time dependent flows, sub-iterations are performed which

will satisfy continuity for each physical step in time[30]. The Navier-Stokes equation for inviscid flows is redefined as:

$$\frac{\partial \vec{U}}{\partial t} + \frac{\partial \tilde{\vec{E}}}{\partial \xi} + \frac{\partial \tilde{\vec{F}}}{\partial \eta} + \frac{\partial \tilde{\vec{G}}}{\partial \zeta} = J \qquad \textbf{3.28}$$

The artificial compressibility algorithm solves only the continuity and momentum equations in GASP. The vectors, **U, E, F** and **G** now become

$$\tilde{U} = J^{-1}\begin{bmatrix} p \\ u \\ v \\ w \end{bmatrix}$$

$$\tilde{E} = J^{-1}\begin{bmatrix} \beta^2 \hat{U} \\ \hat{U}u + p\xi_x \\ \hat{U}v + p\xi_y \\ \hat{U}w + p\xi_z \end{bmatrix}$$

$$\tilde{F} = J^{-1}\begin{bmatrix} \beta^2 \hat{V} \\ \hat{V}u + p\eta_x \\ \hat{V}v + p\eta_y \\ \hat{V}w + p\eta_z \end{bmatrix}$$

$$\tilde{G} = J^{-1}\begin{bmatrix} \beta^2 \hat{W} \\ \hat{W}u + p\zeta_x \\ \hat{W}v + p\zeta_y \\ \hat{W}w + p\zeta_z \end{bmatrix} \qquad \textbf{3.29}$$

3.3.2 Preconditioned Roe

The preconditioned Roe flux is applied to the compressible Navier-Stokes equations. The standard Roe flux will first be discussed and then the preconditioned matrix by Weiss and Smith[6]. The Roe flux is based on a solution to a linear problem

approximating the Riemann problem. The Riemann problem arises at the cell interface. For example, if the state vectors on the left, U_l and right, U_r, sides of the interface are given, the flux through the cell must some how be determined. The Roe solver uses a characteristic decomposition of the discontinuity to obtain an answer. A system $U_t + (F(U))x = 0$ with Riemann problem U_l and U_r states becomes $U_t + AU_x = 0$, where A is the averaged matrix of U_l and U_r states, called Roe averages. The averaged matrix is chosen to satisfy certain conditions of the nonlinear Rieman problem. The Roe flux is then given as

$$F_{i+\frac{1}{2}} = \frac{F(U^l_{i+\frac{1}{2}}) + F(U^r_{i+\frac{1}{2}})}{2} - \frac{1}{2}\left|\tilde{A}\right|\left[U^l_{i+\frac{1}{2}} - U^r_{i+\frac{1}{2}}\right] \qquad \textbf{3.30}$$

The Roe flux is preconditioned so that it can handle low-speed flows. The equivalent artificial viscosity matrix for the preconditioned system is $|PA|$. The eigensystem for **PA** is different from **A** since the preconditioning modifies the wave speeds of the traveling disturbances[31]. The modified Roe flux is now

$$F_{i+\frac{1}{2}} = \frac{F(U^l_{i+\frac{1}{2}}) + F(U^r_{i+\frac{1}{2}})}{2} - \frac{1}{2}P^{-1}\left|\tilde{P}\tilde{A}\right|\left[U^l_{i+\frac{1}{2}} - U^r_{i+\frac{1}{2}}\right] \qquad \textbf{3.31}$$

The modified flux is based on the matrix of Weiss and Smith[6]. The preconditioning is coupled with a dual-time stepping approach in order to solve time accurate flows. The algorithm can handle variable density as well as constant density flows. For a more thorough description of the Roe and the preconditioned Roe fluxes please see References 6 and 18.

3.4 Turbulence Models

In the study of turbulent flows the ultimate objective is to obtain a tractable quantitative model that can be used to calculate quantities of interest and practical relevance[16]. The problem of modeling the Reynolds stress terms is very difficult. Some models work better than others for solving specific flows. The two turbulence models compared and analyzed for low-speed flow over a bluff body are the Spalart-Allmaras model and the Wilcox k-ω (1998) model. These provide a good a comparison because they are two different levels of turbulence models with varying complexity and accuracy.

The models used in this research are turbulent viscosity models. These models are based on the Boussinesq approximation and provide closure using a velocity scale and a length scale. The viscous shear stresses become:

$$\begin{aligned}
\tau_{xx} &= \frac{2}{3}(\mu+\mu_t)\left(2\frac{\partial u}{\partial x}-\frac{dv}{\partial y}-\frac{\partial w}{\partial z}\right)-\frac{2}{3}\rho K \\
\tau_{yy} &= \frac{2}{3}(\mu+\mu_t)\left(2\frac{\partial v}{\partial y}-\frac{du}{\partial x}-\frac{\partial w}{\partial z}\right)-\frac{2}{3}\rho K \\
\tau_{zz} &= \frac{2}{3}(\mu+\mu_t)\left(2\frac{\partial w}{\partial z}-\frac{dv}{\partial y}-\frac{\partial u}{\partial x}\right)-\frac{2}{3}\rho K
\end{aligned} \qquad \textbf{3.32}$$

$$\begin{aligned}
\tau_{xy} &= \tau_{yx} = \frac{2}{3}(\mu+\mu_t)\left(\frac{\partial u}{\partial y}+\frac{\partial v}{\partial x}\right) \\
\tau_{xz} &= \tau_{zx} = \frac{2}{3}(\mu+\mu_t)\left(\frac{\partial u}{\partial z}+\frac{\partial w}{\partial x}\right) \\
\tau_{yw} &= \tau_{wy} = \frac{2}{3}(\mu+\mu_t)\left(\frac{\partial w}{\partial y}+\frac{\partial v}{\partial z}\right)
\end{aligned} \qquad \textbf{3.33}$$

The shear stresses are from the momentum terms of the viscous fluxes found in equation [3.14]. The new variables introduced above are the turbulent eddy viscosity, μ_t and the turbulent kinetic energy, K. For a one equation model K is not solved for. The two

equation models develop methods for solving both quantities. The heat fluxes from the energy equation, q_x, q_y and q_z are defined for two-equation models:

$$\begin{aligned} q_x &= -(k + k_t)\frac{\partial T}{\partial x} - \left(\mu + \frac{\mu_t}{\mathrm{Pr}_k}\right)\frac{\partial K}{\partial x} \\ q_y &= -(k + k_t)\frac{\partial T}{\partial y} - \left(\mu + \frac{\mu_t}{\mathrm{Pr}_k}\right)\frac{\partial K}{\partial y} \\ q_z &= -(k + k_t)\frac{\partial T}{\partial z} - \left(\mu + \frac{\mu_t}{\mathrm{Pr}_k}\right)\frac{\partial K}{\partial z} \end{aligned} \qquad \textbf{3.34}$$

Two more new terms come out, the turbulent thermal conductivity, k_t and the turbulent kinetic energy closure coefficient, Pr_K. Again, the one equation models do not solve for K. One-equation models, like the Spalart-Allmaras model, use the Prandtl mixing length model and set the turbulent velocity scale to a specified quantity. The result is a single equation that solves for a turbulent viscosity type variable, $\tilde{\nu}$. Two-equation models, like the Wilcox k-ω (1998) model, have an additional equation that models the length scale. The two-equation model in this research uses the following equation for a length scale:

$$l_t = \frac{\sqrt{TKE}}{\omega} \qquad \textbf{3.35}$$

where TKE is the turbulent kinetic energy and ω is the turbulent frequency

3.4.1 The Spalart-Allmaras Model

The first turbulence model to be discussed balances ease and cost of use with accuracy. Spalart and Allmaras[9] devised a one equation model for the transport of the turbulent viscosity, μ_t. The Spalart-Allmaras turbulent eddy viscosity is given by

$$\mu_T = \rho\tilde{\nu}f_{v,1} \qquad \textbf{3.36}$$

where f_{v1} is the damping function of the kinematic viscosity ratio and $\tilde{\nu}$ is an artificial viscosity-like term called the Spalart variable. The model equation is of the form

$$\overline{\frac{D\nu_T}{Dt}} = \nabla \cdot (\frac{\nu_T}{\sigma_\nu} \nabla \nu_T) + S_\nu \qquad \textbf{3.37}$$

which expands to:

$$\frac{\partial \tilde{\nu}}{\partial t} + \frac{\partial (\tilde{\nu} u)}{\partial x} + \frac{\partial (\tilde{\nu} v)}{\partial y} + \frac{\partial (\tilde{\nu} w)}{\partial z} = \frac{\partial \tau_x^\nu}{\partial x} + \frac{\partial \tau_y^\nu}{\partial y} + \frac{\partial \tau_z^\nu}{\partial z} + C_{b1} S_\nu \tilde{\nu} - C_{w1} f_w \left(\frac{\tilde{\nu}}{d} \right)^2 + \frac{1}{\sigma} \left[\nabla \cdot \vec{V} \right] + \frac{C_{b2}}{\vartheta} (\nabla \tilde{\nu})^2 \qquad \textbf{3.38}$$

Where S is the source term that depends on the laminar and turbulent viscosities, ν and ν_T; the mean vorticity, Ω; the turbulent viscosity gradient, $\nabla \nu_T$; and the distance to the nearest wall, d [17]. The diffusion terms are defined as functions of the Spalart variable:

$$\tau_x^\nu = \left(\frac{\nu + \tilde{\nu}}{\sigma} \right) \frac{\partial \tilde{\nu}}{\partial x}$$

$$\tau_y^\nu = \left(\frac{\nu + \tilde{\nu}}{\sigma} \right) \frac{\partial \tilde{\nu}}{\partial y}$$

$$\tau_z^\nu = \left(\frac{\nu + \tilde{\nu}}{\sigma} \right) \frac{\partial \tilde{\nu}}{\partial z}$$

For a more thorough discussion of the development of this model and the full definition of the source and closure terms, review the paper by Spalart and Allmaras (1994)[9] and the Reference [30].

3.4.2 The Wilcox k- ω (1998) Model

The second turbulence model used in this research is the two-equation Wilcox k-ω (1998) model. This model handles adverse pressure gradients well and is integrated through the laminar sublayer without a damping function.

In two-equation models, transport equations are solved for two turbulence quantities. The first quantity used in most solutions is common to two-equation models, the turbulent kinetic energy K, found in equations [3.35] and [3.37]. There are many choices for the second quantity. In the k-ω model, the second quantity, ω, can be referred to as the ratio of the rate of dissipation, ε, per unit of turbulence kinetic energy, κ. It is also called the turbulent frequency and has dimensions of $(\text{time})^{-1}$. The Wilcox k-ω model equations use the following closure equations: the eddy viscosity, turbulence kinetic energy and specific dissipation rate.

Eddy Viscosity

$$\mu_T \equiv \frac{\rho k}{\omega} \qquad \textbf{3.39}$$

Turbulence Kinetic Energy

$$\rho\frac{\partial k}{\partial t} + \frac{\partial(\rho U_j k)}{\partial x_j} = \frac{\partial \tau_{ij}^K}{\partial x_j} - C_{D_K}\rho k\omega + C_{P_\varepsilon}\left[\mu_t S^2 - \frac{2}{3}\rho K(\nabla\cdot\vec{V})\right] \qquad \textbf{3.40}$$

Specific Dissipation Rate

$$\rho\frac{\partial \omega}{\partial t} + \frac{\partial(pU_j\omega)}{\partial x_j} = \frac{\partial \tau_{ij}^k}{\partial x_j} - \beta\rho\omega^2 + \frac{\partial}{\partial x_j}\left[(\mu + \sigma\mu_T)\frac{\partial \omega}{\partial x_j}\right] \qquad \textbf{3.41}$$

Where S^2 is the strain invariant defined by: $S^2 = (u_{i,j} + u_{j,i})u_{i,j} - \frac{2}{3}(\nabla \cdot \vec{V})$. The additional auxiliary relations for the length scale and dissipation rate are:

$$l = \frac{\sqrt{k}}{\omega} \quad \textbf{3.42}$$

$$\varepsilon = \omega k \quad \textbf{3.43}$$

Chapter 4: Boundary Conditions and Computational Grids

Choosing the appropriate boundary condition for a surface is an important part in CFD modeling. The boundary conditions influence how the governing equations are solved and make each problem unique. The boundary conditions are applied to each surface of the computation grid.

The paradox involved in creating a computation grid is using discretized volumes small enough to resolve the flow physics while maintaining an overall number of cells that use time, memory and CPU efficiently. Large volume cells will be unable to accurately predict flow behavior on both large and small scales because of the distance with which information is passed. On the other hand, while small volumes are desirable, the computation time will be greatly increased as well as the CPU needed for calculations. Therefore, for the most effective computation grid, a balance between size and efficiency must be found

This section discusses the selection of appropriate boundary conditions for flow over square cylinders and the generation of computation grids used in this study.

4.1 Boundary Conditions

4.1.1 Single-Cylinder Configuration

The computational domain for the 2-D square-cylinder consists of a circular far-field boundary around the cylinder. Boundary conditions were applied on the surface of

cylinder, the inflow boundary upstream of the cylinder, the outflow boundary downstream of the cylinder and the exterior boundaries on the far-field flow. A schematic of the grid is shown in Figure [4.1].

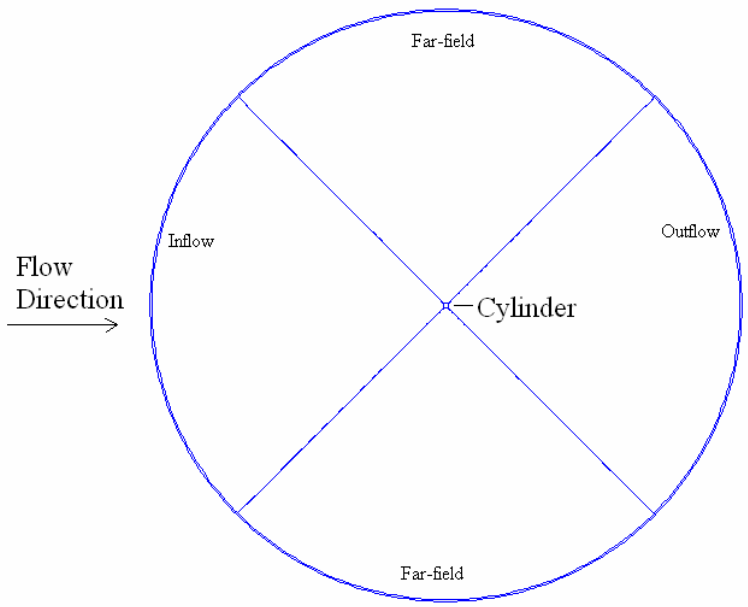

Figure 4.1 Computation grid of the single-cylinder configuration.

Cylinder Surface

The boundary condition applied to the surface of the cylinder was a no-slip (u=v=w=0), adiabatic wall ($\delta T/\delta n=0$) condition. The no-slip adiabatic condition is used for viscous flows on a solid wall boundary. The temperature gradient at the surface is set to zero by extrapolating the pressure and densities. The surface is assumed to be smooth.

Inflow/Outflow

The freestream conditions upstream of the cylinder were known. On the inflow boundary faces, pressure is extrapolated and the remaining boundary values are set according to the specified freestream conditions. For outflow boundaries where the flow

is moving out of the boundary, the back pressure is set according to the known freestream conditions. All other boundary values are extrapolated from the first interior cell.

Far-Field

First-order extrapolation was applied to the remaining sides, the top and bottom surfaces of the grid. These surfaces do not represent a physical location and therefore the data must be extrapolated from the conditions set at the boundary cells to the ghost cells. This results in a zero gradient at the boundary.

4.1.2 Three-Cylinder Configuration

The computational domain for the 2-D three-cylinder formulation is based on the turbulence generating experiment discussed in Chapter 2. The cylinders extended the horizontal length of the tunnel and as a result the grid was treated to be 2-D. Boundary conditions were applied at the inflow, outflow, cylinder surfaces and the upper and lower tunnel walls. A schematic of the computation grid can be found in Figure [4.2]. The dimensions are shown in Chapter 1 (Figure 1.2).

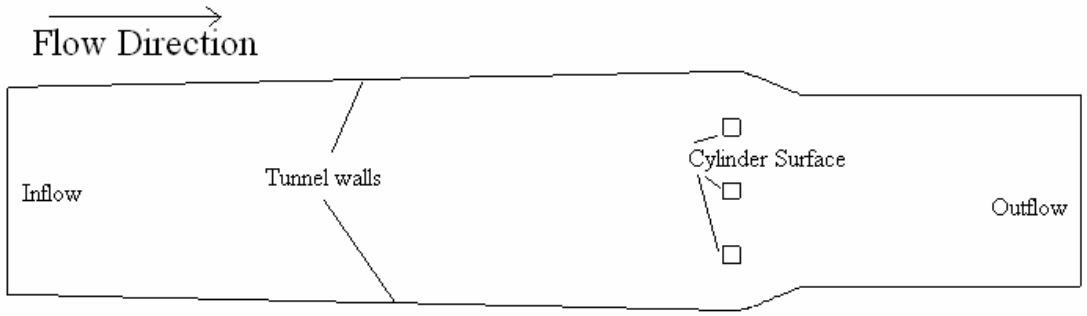

Figure 4.2 Computation grid for the three-cylinder configuration.

Cylinder Surface and Tunnel Walls

The boundary condition applied to the surface was a no-slip (u=v=w=0), adiabatic wall ($\delta T/\delta n=0$) condition. The no-slip adiabatic condition is used for viscous flows on a solid wall boundary. The temperature gradient at the surface is set to zero by extrapolating the pressure and densities. The surface is assumed to be smooth.

Inflow/Outflow

The freestream flow is know upstream of the cylinders. A boundary condition is applied at the inflow to simulate the known subsonic flow conditions. On the inflow boundary faces, pressure is extrapolated and the remaining boundary values are set according to the specified freestream conditions. For outflow boundaries, the back pressure is set according to the specified freestream conditions. All other boundary values are extrapolated from the first interior cell.

4.2 Computational Grids

The multi-block grids generated were done using Gridgen[12] version 15.02. GASP requires a structured grid to be imported using Plot3D format. This study is two-dimensional, but GASP solves three-dimensional finite volume grids. Therefore, a 2-D grid was created in Gridgen and then imported into GASP. Once imported, the grid was extruded in one dimension to create volumes. The two computation grids used in this study were comprised of simple O-grids and H-grids. For the three-cylinder configuration, an H-grid filled in the area between the O-grid and the tunnel walls. An O-grid was extruded from the surface of each square. The grid was extruded using a

hyperbolic tangent formula. The formula increased the grid spacing more efficiently than a linear stepping formula would. The initial spacing for the grid in the boundary layer on the square cylinders was determined using the following formula:

$$\Delta y = \frac{0.7L}{\sqrt{\mathrm{Re}_L}} \qquad \textbf{4.1}$$

The spacing accuracy can be verified by calculating $y^+ \equiv \frac{yu^*}{\nu}$. A spacing of y^+ less than one (0.667) was calculated for both configurations, which is an acceptable value. The spacing at the corners is slightly larger than the spacing normal to the cylinder surfaces due to the fact that the grid was extruded away from the faces of the cylinder.

After the grids were imported into GASP, they were sequenced twice within GASP. Sequencing removes every other grid point from the original (fine) grid. Sequencing develops the flow quicker but trades accuracy. Once the flow is developed, the finer grid is used and accuracy is obtained. Sequencing can increase the rate of convergence by solving on coarser grids to allow a problem to set up and then solving on the fine grid for accuracy. Using sequenced grids decreases the time and CPU needed.

Both configurations were initially run as steady-state to allow the flow to setup and to determine the grid size to be used in the unsteady calculations.

4.2.1. Single-Cylinder Configuration

The single cylinder computational grid is an O-grid that was extruded off the surface of the cylinder. The grid extended 40 diameters from the surface. The spacing

near the walls was 1 x 10^{-5} and at the corners was 1.414 x 10^{-4}. The grid was clustered around the block in order to capture boundary layer effects.

The grid used for the single-cylinder calculations was sequenced twice to produce three grids: fine, medium and coarse. The fine grid had 55,328 cells. Confidence in the grid size was established by outputting a parameter from each grid sequence and determining the percent difference between grids. The drag coefficient was integrated over the surface of the cylinder for each sequence and plotted in Figure [4.3]. The drag coefficient for the coarse grid was 7.9% less than that of the fine grid. The medium grid differed from the fine grid by 0.5%. Therefore, confidence is established in the size of discretized volumes in the fine grid.

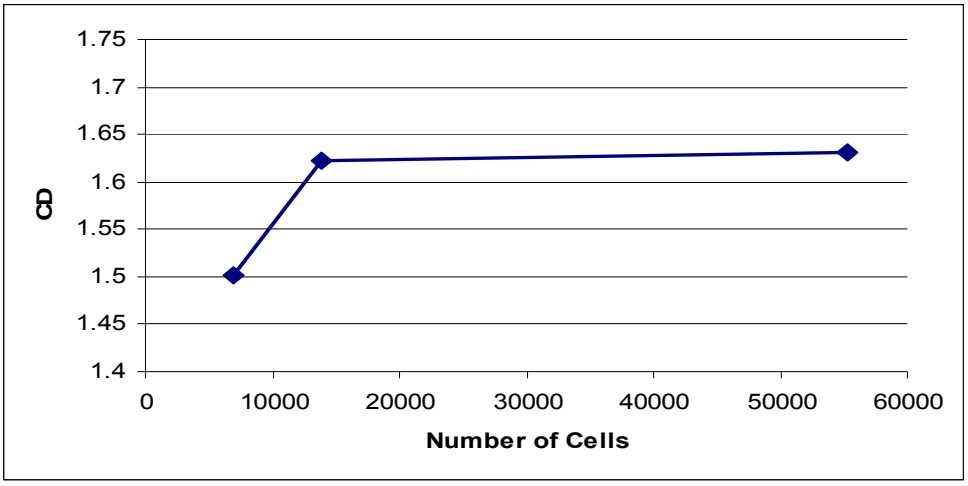

Figure 4.3 Grid convergence for the single-cylinder configuration

4.2.2 Three-Cylinder Configuration

The computational grid for the three cylinders was predominately an H grid with an O-grid around the cylinders. The O-grid was extruded off the surface of each cylinder

and the H-grid was filled in around the cylinders and the remaining portions of the grid. The grid was clustered around the surface of each cylinder and on the surface of the tunnel walls in order to account for the boundary layer. The spacing near the walls was the same as the single-cylinder configuration. The three-cylinder configuration had approximately 40,000 cells.

The three-cylinder configuration was sequenced once to create two grids, fine and coarse. Grid convergence was tested in the same manner as the single-cylinder configuration. The drag coefficient of the middle cylinder is 1.5% smaller on the coarse grid. As a result, the fine grid was concluded to have small enough volumes to describe the flow. Figure [4.4] shows the grid convergence for the three-cylinder configuration.

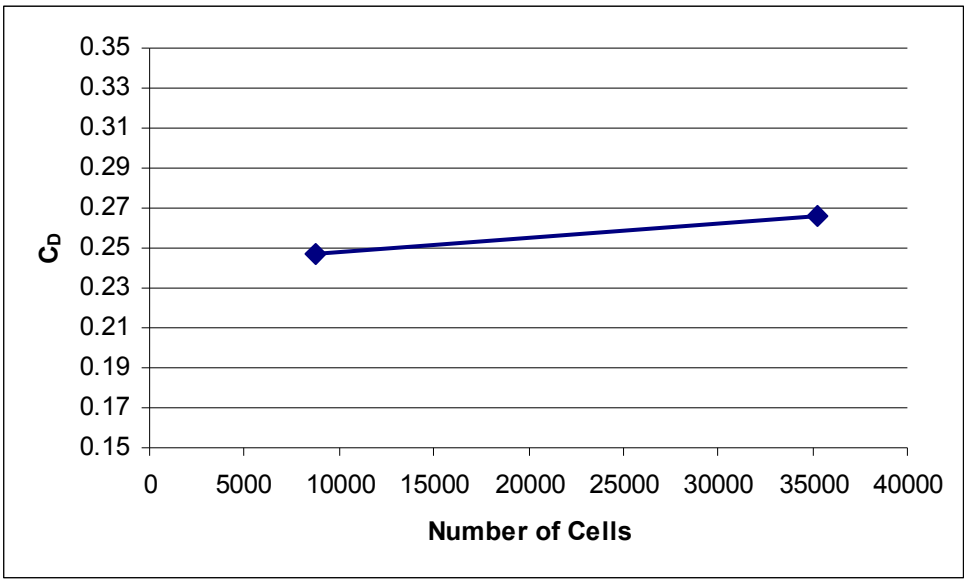

Figure 4.4 Grid Convergence for the three-cylinder configuration.

4.2.3 Convergence Criteria

Two methods of convergence criteria were studied. One method involved the number of inner cycles computed for each time-step. The other method applied only to the artificial compressibility algorithm. An optimum value of beta was found by varying the constant that is multiplied by the velocity squared. A summary of the results for the convergence criteria can be found in Chapter 5.

4.2.3.1 Inner Cycles

Time accurate flows require the specification of the number of cycles used for solving each time step. Cycles of 5 and 10 were used for the three-cylinder case and 10, 20 and 30 for the single-cylinder case. Preferably, 5 or 10 inner cycles or iterations would be used for quicker CPU times. The number of inner cycles is connected to the physical time-step; using a combination of the largest time-step possible and lowest number of inner cycles is desired. While using the maximum time-step allowable (i.e. the solution is numerically stable), the number of inner cycles was varied and the results presented. The integrated force data was used in determining convergence. Each formulation was run for the same time period with various inner cycles. The resultant force data was recorded and compared.

4.2.3.2 Beta

Beta, β, is equal to a constant multiplied by the velocity squared. It is a compressibility parameter in the artificial compressibility algorithm. As a rule of thumb a

good value for β is $5*V^2$ where V is the free-stream velocity. Three values for β were tested on the three-cylinder configuration, $\beta = 5* V^2$, $\beta = 10* V^2$ and $\beta = 100*V^2$. The result from the three-cylinder configuration was then used in the single-cylinder configuration.

Chapter 5: Results and Discussion

5.1 Overview

In this section, numerical results for both the single-cylinder and the three-cylinder configurations are presented and compared with experimental data. The results for the single-cylinder are given first and then the three-cylinder configuration results. In each section, results are shown that demonstrate how well the selected turbulence models and low-speed algorithms represent the actual flow physics and how well the predictions correlate with experimental data. Experimental data has been collected for both configurations and was discussed in Chapter 2. Since the flow is unsteady, a time-accurate solution is presented.

Flow field visualization, force data and the Strouhal number (St) will be presented for both configurations. Other results such as the pressure coefficient (Cp), mean velocity magnitude, turbulence intensity, eddy viscosity ratio and convergence criteria will also be given for one configuration or the other. Each of these categories will be discussed before the results are presented.

5.1.1. Flow Field Visualization

The flow field is visualized using vorticity contours. The contours for each plot have the same scale and were output directly from GASP. The contours show the vorticity distribution at a peak in the C_L data. This was done in an attempt to have data at approximately the same location in the shedding period for each plot for quality

comparisons. All of the contours show a high pressure region in front of each cylinder, separation off the leading edge and periodic vortical shedding. Distinct vortices are formed downstream of the cylinders.

5.1.2 Aerodynamic Force Coefficients and Strouhal Number

The X (streamwise) and Y (transverse) forces were integrated over each cylinder for an arbitrary time period and then converted to C_D and C_L. The mean C_D values were compared to each other and the experimental results when available. A time history of the force data was also used to determine the frequency of shedding. A Fast Fourier Transform (FFT) of the force data was computed in order to obtain the frequency domain. The maximum frequency was then used to calculate the Strouhal number using equation [5.1].

$$St = \frac{nD}{V} \qquad \textbf{5.1}$$

where n is the frequency of the vortex shedding, D is the side length of the cylinder and V is the free stream velocity

5.1.3 Mean Pressure Coefficient on the Cylinder Surface

The mean pressure coefficient, C_P was calculated over the surface of the single-cylinder configuration only because of the availability of experimental data. In order to focus on the effect the flux algorithms have on the C_P, the turbulence models were not compared. Instead, only the two low-speed algorithms are focused on. The Spalart-Allmaras model was used while varying the flow algorithm, because it produced the most repetitive data that was consistent with the experimental force data. The mean C_P was

measured from the center of the windward face, moving clockwise around the square cylinder, see Figure 5.1.

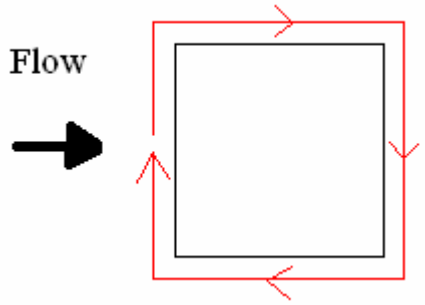

Figure 5.1 The Direction of measurement of C_P.

5.1.4 Mean Velocity Magnitude and Turbulence Quantities

Predictions will be presented for the velocity magnitude, turbulence intensity and the eddy viscosity/laminar viscosity ratio for the three-cylinder configuration in order to compare with experimental data. The data was taken 0.5 m downstream of the cylinders in a vertical plane. A vertical line of data points 0.5 m downstream were output from GASP each physical time step. The data that was output was the mean velocity magnitude, the turbulent kinetic energy, k, and the eddy viscosity to laminar viscosity ratio. The parameters were averaged over the entire run time.

The two measures of turbulence analyzed were the viscosity ratio and the turbulence intensity. The viscosity ratio is the ratio of eddy viscosity to laminar viscosity. This parameter describes turbulence production and development in the flow. The amount of turbulence present increases with the ratio. By comparing the ratio for each case, an appreciation for the turbulent behavior can be achieved.

The turbulence intensity is calculated using k and the local velocity, which was output from GASP over several time periods. The data was averaged over the run time. Equation [5.2] calculates the turbulence intensity from the k and the local velocity, U.

$$ti = \frac{\sqrt{0.8 * k}}{U} \qquad \textbf{5.2}$$

5.2 Single-Cylinder

Results are presented showing comparisons with experimental data, as well as comparisons between the different flow algorithms and turbulence models for the single-cylinder configuration. This section will discuss the following: flow field visualization, aerodynamic force coefficients, mean pressure coefficient, Strouhal number and an inner cycle convergence test.

5.2.1 Flow Field Visualization

An instantaneous snapshot of vortex shedding produced by all the formulations can be seen in Figure 5.2 (a)-(d). Each plot shows the vorticity distribution at a peak in the C_L cycle (force history data can be seen in Figure 5.4). The contours range from 0 to 2000 s^{-1}. All four figures show similar results, a large high pressure region in front of the cylinder, separation immediately off the leading edge and periodic shedding in the wake. Visually, one can see a difference between the results with the Spalart-Allmaras model and the Wilcox k-ω model. The Wilcox k-ω simulations produced stronger intensity vortices than the Spalart-Allmaras model. Also, lateral vortices can be found in the separation region of the Wilcox k-ω model contours. The high pressure region in front of the square cylinder oscillates slightly in phase with the oscillations produced by the

vertical shedding behind the cylinder. The flow is low speed, so the behavior downstream is expected to affect the upstream flow. Overall, the basic physics of the flow was captured in all four cases.

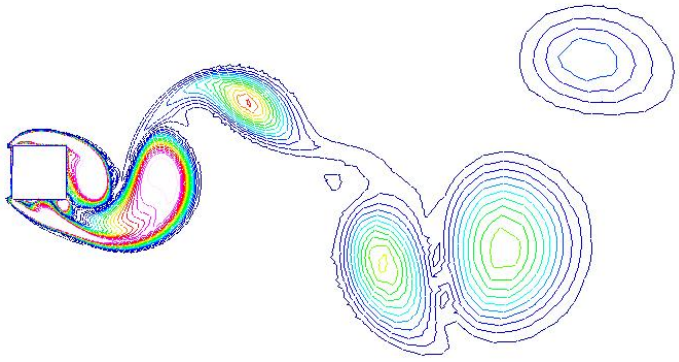

Figure 5.2(a) Spalart Allmaras model with artificial compressibility.

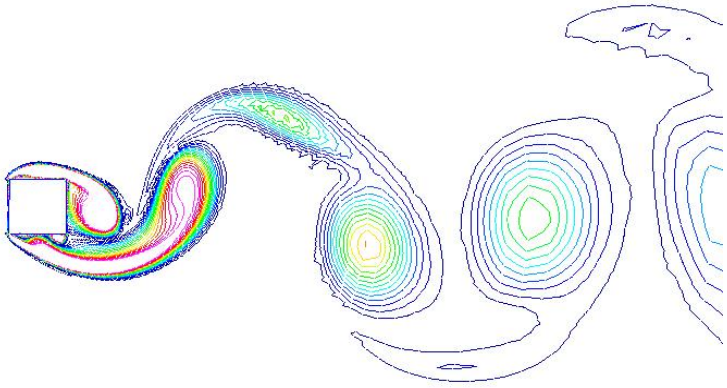

Figure 5.2(b) Spalart Allmaras model with preconditioned Roe.

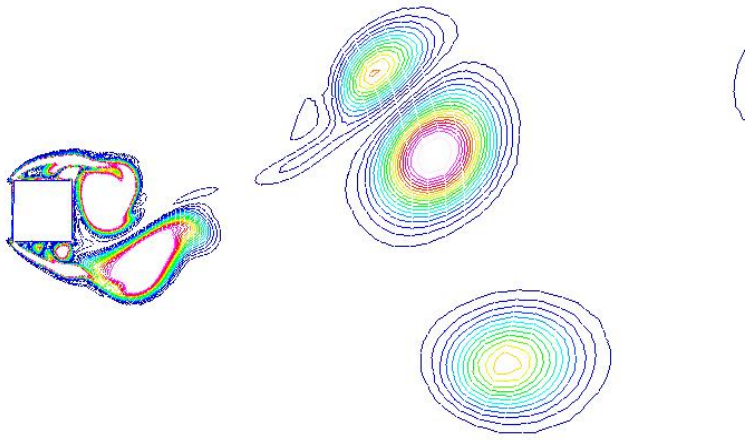

Figure 5.2(c) Wilcox k-ω model with artificial compressibility

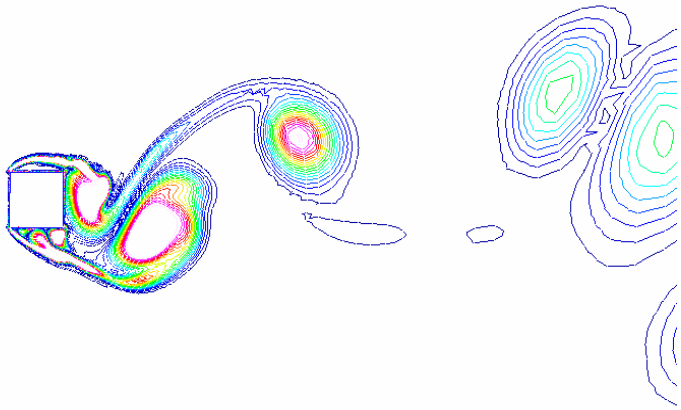

Figure 5.2(d) Wilcox k-ω model with preconditioned Roe.

Figure 5.2 Predicted vorticity contours of the single-cylinder configuration.

5.2.2 Aerodynamic Force Coefficients: C_D (X-Force) and C_L (Y-Force)

The mean C_D and mean C_L data can be found in Table 5.1. The mean drag coefficients for the Spalart-Allmaras model agree more closely with experimental data than the drag coefficients for the Wilcox k-ω model. The results for the Spalart-Allmaras

model are 2-3% lower than the experimental data. All formulations under-predict the mean drag coefficient except the Wilcox k-ω model with the artificial compressibility algorithm, which over-predicts the experimental results by 4%. The low-speed algorithm mean force predictions did not vary significantly when the Spalart-Allmaras model was used. The C_D and C_L data was averaged over several time periods, but, as can be seen from Figures 5.3 and 5.4, the forces did not behave in exact sinusoidal patterns. Therefore, the time to complete a period varied as did the height of each peak. Thus, when C_L was averaged, it was not exactly zero, as would be expected theoretically because the cylinder is not angled with respect to the flow.

Table 5.1Mean C_D and C_L predictions for the single-cylinder configuration.

Formulation	Mean C_D	%Error of Mean C_D and Lee[13]	Mean C_L
Spalart-Allmaras			
Preconditioned Roe	1.986	2.66	-0.0403
Artificial Compressibility	1.995	2.19	-0.0178
Wilcox k-ω			
Preconditioned Roe	1.871	8.29	-0.029
Artificial Compressibility	2.130	4.42	-0.026
Experimental			
Lee[13]	2.04	-	
Norberg[14]	2.10		

The magnitude of the oscillatory forces and the frequencies show a variation between the results from different turbulence models. To better visualize this, Figures 5.3 and 5.4 show sample increments in the time history of both the lift and drag coefficients with different flux schemes and turbulence models. The C_D plot shows that the results do not follow a simple pattern and that the data is inconsistent between both turbulence

models and algorithms. Because of the chaotic and inconsistent behavior of C_D, only the mean value was compared to experiment, refer to Table 5.1. Figure 5.3 shows that a simple time-dependent C_D pattern is hard to achieve using different algorithms and turbulence models. But, based on the information given in Table 5.1, the average C_D predicted for all four formulations was off by no more than 8% compared to experiment.

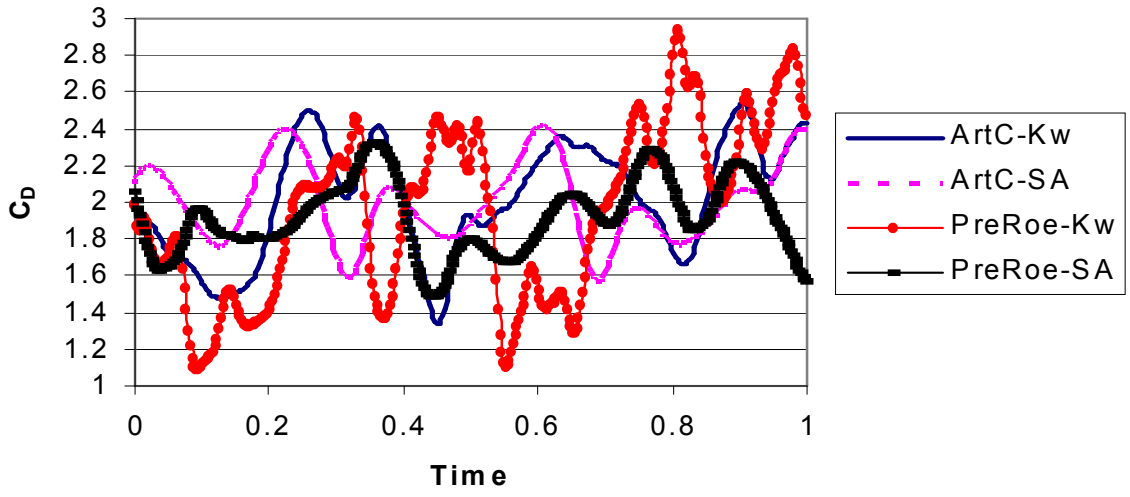

Figure 5.3 Drag coefficient behavior over arbitrary time for the single-cylinder configuration.

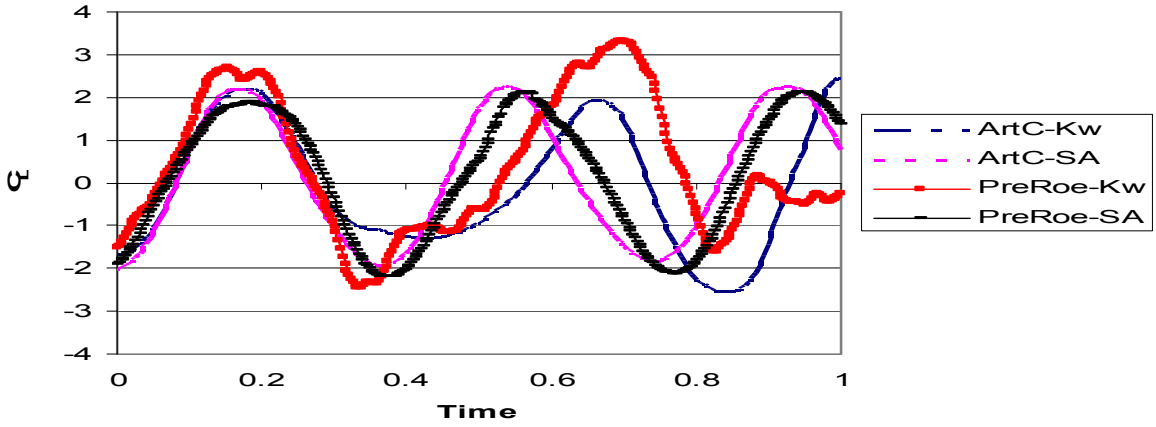

Figure 5.4 Lift coefficient behavior over arbitrary time for the single-cylinder configuration

The C_L results plotted in Figure 5.4 are almost sinusoidal. When the C_L data is averaged, it should be approximately zero since the cylinder is not angled with respect to the flow. As was shown and explained earlier, the averaged data is close but not exactly zero. The information that can be extracted from the C_L results plot is the frequencies of vortex shedding and differences between the magnitude ranges of the four formulations. The two cases run with the artificial compressibility algorithm have the same range in magnitude, but the frequencies are different. In the plot, the artificial compressibility algorithm with the Wilcox k-ω model shows slightly more than one oscillation wave, whereas the artificial compressibility algorithm with the Spalart-Allmaras model has slightly more than two waves. The two cases with preconditioned Roe do not match each other in frequency or magnitude range. However, one of those cases, the preconditioned Roe algorithm with the Spalart-Allmaras model, has peak magnitudes close to the artificial compressibility algorithm with the Spalart-Allmaras turbulence model. The frequencies are similar as well; both cases produce just over two waves for the arbitrary time. The peak magnitude in the amplitudes of the experimental lift coefficient results were between 2 and 2.5. All of the cases except the one with the Wilcox k-ω model and the preconditioned Roe algorithm are close to the experimental amplitudes. It can be deduced that the cases run with the Spalart-Allmaras model produce waves with similar frequencies and ranges in C_L magnitudes.

Looking at both plots, the case using the preconditioned Roe algorithm with the Wilcox k-ω model over-predicts the forces when compared to the other cases. The results from the other three approaches stay approximately within the same force values.

5.2.3. Strouhal Number

The St was calculated using Equation 5.1. Table 5.2 lists the results from the calculations and the experimental data. The Spalart-Allmaras results are in good agreement with the Norberg experiment. The St predictions for the Wilcox k-ω model formulations vary greatly from the experimental data (20+% smaller). There is also a higher uncertainty in the St predictions for the k-ω model, since the St value is very sensitive to the range of data used to compute it and the k-ω model predicted chaotic oscillations. The amount of uncertainty with the Wilcox k-ω turbulence model could be a result of the non-repetitive behavior of the forces. The St predictions are consistent with the force results (specifically, frequency results) found in Figures 5.3 and 5.4. The Wilcox k-ω model greatly under-predicts St, while the Spalart-Allmaras model results are only one percent less than the experimental value.

Table 5.2 Strouhal Number predictions for the single-cylinder configuration

Formulation	St
Spalart-Allmaras	
Preconditioned Roe	0.130
Artificial Compressibility	0.131
Wilcox k-ω	
Preconditioned Roe	0.118
Artificial Compressibility	0.104
Experimental	
Lee[13]	0.124
Norberg[14]	0.132

5.2.4. Mean Pressure Coefficient on Surface

The mean pressure coefficient was calculated for the Spalart-Allmaras model only. The reason for this was stated earlier. Figure 5.5 shows that the CFD data followed the same trend as the experimental data. The magnitudes of the predictions differed from experiment in two locations, the upper back corner and the lower back corner of the cylinder, this could be a result of the slightly larger initially grid spacing at the corners. The preconditioned Roe results were slightly lower than the artificial compressibility result on the top and bottom sides of the cylinder. The discrepancies could be a result of the small time period over which the CFD data was averaged or the difference between 2-D modeling and 3-D experiment. Both models predict separation at the front corners of the square-cylinder.

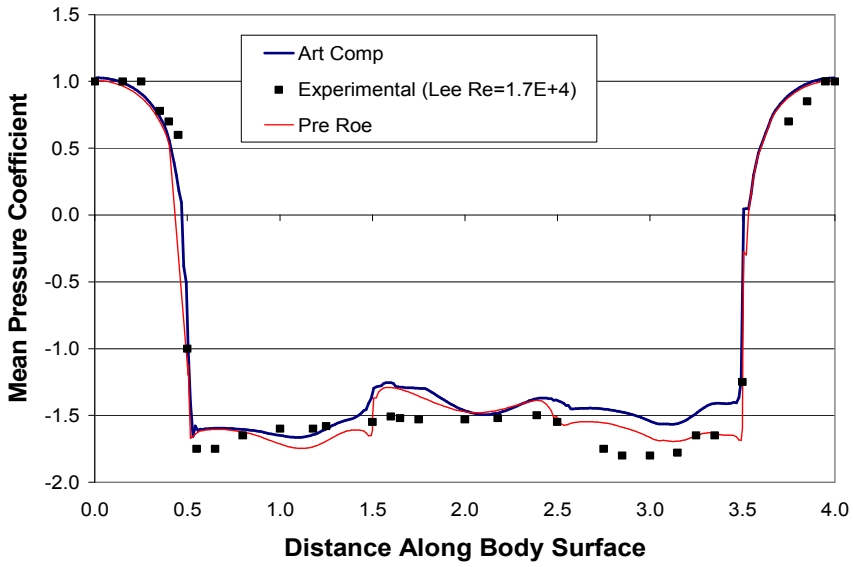

Figure 5.5 Mean pressure coefficient with the Spalat-Allmaras model for single-cylinder configuration.

5.2.5. Inner-Cycle Convergence Test

Several cases were run while varying the number of inner cycles in the dual-time stepping algorithm. Again, only Spalart-Allmaras was used for a turbulence model, while the flux algorithms were compared. Artificial compressibility showed that 10 inner cycles produced different results than 20 and 30 inner cycles. Since 20 and 30 inner cycles do not differ in C_D (and only vary slightly in $C_{L,}$) it can be determined that 20 inner cycles is sufficient when using artificial compressibility. The preconditioned Roe algorithm produced the same pattern of results. In conclusion, both flux algorithms had similar convergence behavior. The results from the inner cycle test can be found in Table 5.3.

Table 5.3 Inner cycle convergence predictions for single-cylinder configuration.

Inner Cycles	C_D
Artificial Compressibility	
10	1.966
20	1.967
30	1.967
Preconditioned Roe	
10	1.949
20	1.984
30	1.984

5.3 Three-Cylinder Configuration

Results are now presented showing comparisons with experimental data, as well as comparisons between the different flow algorithms and turbulence models for the three-cylinder configuration. This section will discuss the following: flow field

visualization, aerodynamic force coefficients, Strouhal number, averaged velocity magnitude, viscosity ratio, turbulence intensity and convergence tests.

5.3.1 Flow Field Visualization

The visualization contours of instantaneous vorticity can be found in Figure 5.6 (a) – (d). The contours produced by the Spalart-Allmaras model can be found in parts (a) and (b), and the contours produced by the Wilcox k-ω model can be found in parts (c) and (d). Each plot shows the vorticity distribution at a peak in the C_L cycle (force history data can be seen in Figure 5.7). The contours range from 0 to 2000. All four approaches show separation off the leading edge. The separation point is not exactly on the corner of the cylinder; it is on the edges of the front face. All four formulations predict a growing boundary layer on the walls of the tunnel with separation and reattachment in between the shed vortices. The intensities of the vortices as they are initially shed from the cylinders, appear to be similar for all four formulations. The intensity of the vortices with the Spalart-Allmaras model does not dissipate as quickly as with the k-ω model. The Wilcox k-ω model predicts that the vorticies disperse and pair sooner than the Spalart-Allmaras model. Overall, the basic physics of the flow was captured by all of the formulations.

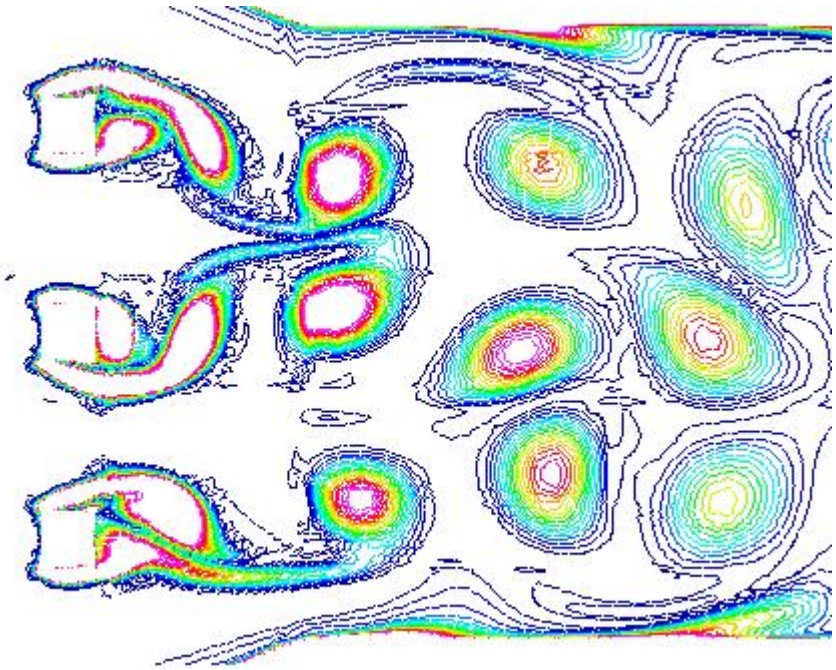

Figure 5.6(a) Spalart-Allmaras model with artificial compressibility.

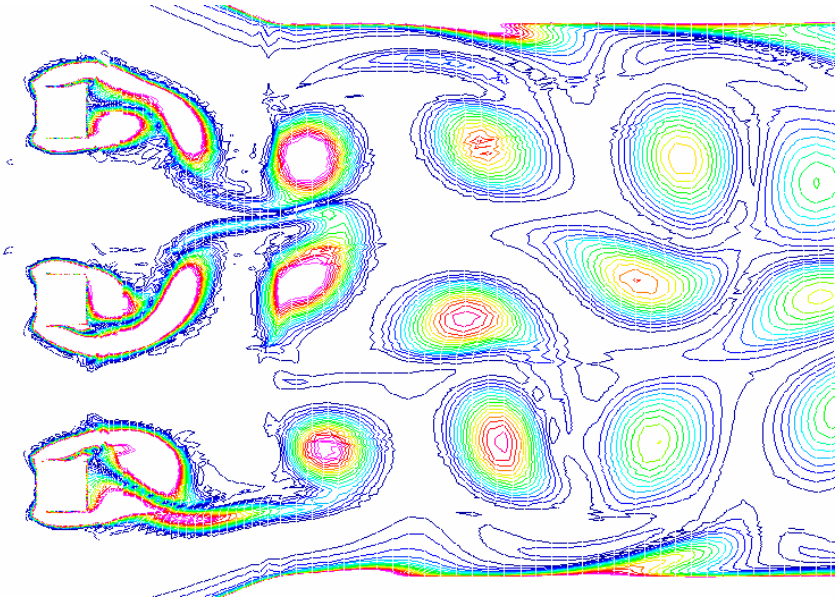

Figure 5.6(b) Spalart-Allmaras model with preconditioned Roe.

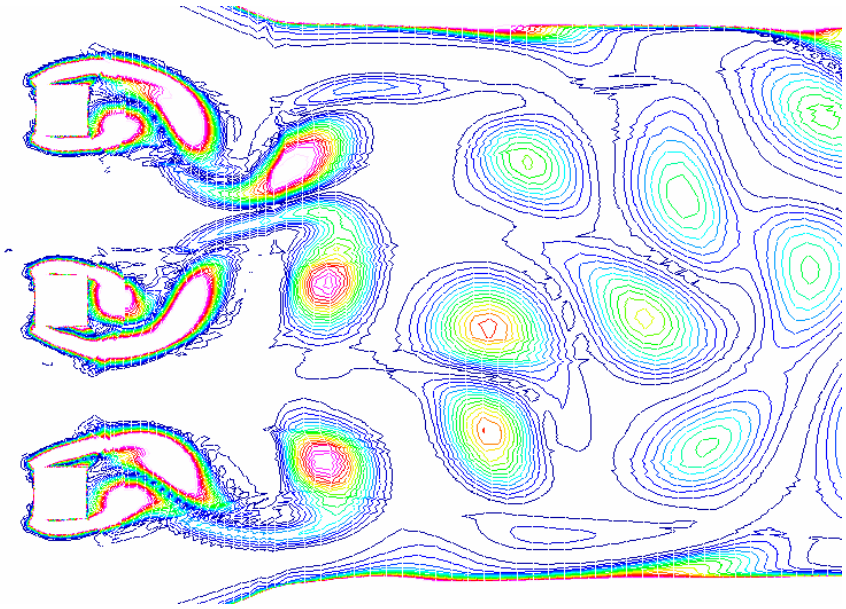

Figure 5.6(c) Wilcox k-ω model with artificial compressibility.

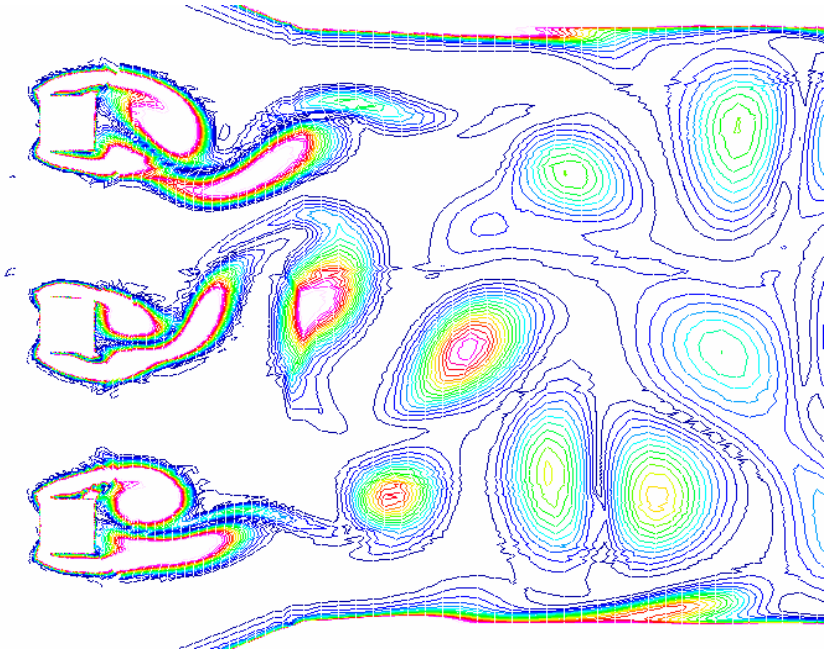

Figure 5.6(d) Wilcox k-ω model with preconditioned Roe.

Figure 5.6 Predicted vorticity contours of the three-cylinder configuration.

5.3.2 Aerodynamic Force Coefficients: C_D (X-Force) and C_L (Y-Force)

The pressures and shears were integrated over the surfaces of each square-cylinder to get lift and drag coefficients. The outer cylinders produced the same force results, therefore they will be discussed as one instead of the upper and lower cylinders. Experimental data for the force history was not available for the three-cylinder configuration. The mean C_D and C_L values can be found in Table 5.4. The Spalart-Allmaras model predicted higher mean C_D values than the Wilcox k-ω model. The algorithm predictions did not vary when the Spalart-Allmaras model was used, but when the Wilcox k-ω model was used, the algorithms did not predict similar mean C_D values. Comparing only the low-speed algorithm, the preconditioned Roe algorithm predicted lower mean C_D than the artificial compressibility algorithm. The mean value of C_L for all four formulations is approximately zero. As with the single-cylinder configuration, the discrepancy with the C_L values not being identically zero could be a result of the time periods over which the data was averaged.

Table 5.4 Mean C_D and C_L values for the middle cylinder of the three-cylinder configuration

Formulation	Mean C_D	Mean C_L
Wilcox k-ω		
Artificial Compressibility	0.283	0.0004
Preconditioned Roe	0.269	0.0001
Spalart-Allmaras		
Artificial Compressibility	0.298	0.0000
Preconditioned Roe	0.297	-0.0005

Figures 5.7 and 5.8 present the C_D and C_L time history predictions for the middle cylinder. The figures are hard to interpret when (arbitrary) time is plotted from 0 to 1. As

a result, the plot shows a smaller time interval, 0.25 – 0.5 for C_D and 0 – 0.5 for C_L. This allows the reader to better visualize the drag behavior of the cylinder.

Figure 5.7 shows that the drag coefficients behave in a repetitive and periodic manner except for the drag predicted by the preconditioned Roe algorithm with the Wilcox k-ω model. The Spalart-Allmaras model predictions have a larger range of oscillation than the Wilcox k-ω model. The Spalart-Allmaras model also predicted better agreement between the two algorithms used. The Wilcox k-ω model with the preconditioned Roe algorithm does not correlate with the other formulations and has a lower C_D value than the other cases. The Wilcox k-ω model predicts irregular pattern. The oscillation periods lengthen when the preconditioned Roe algorithm is used.

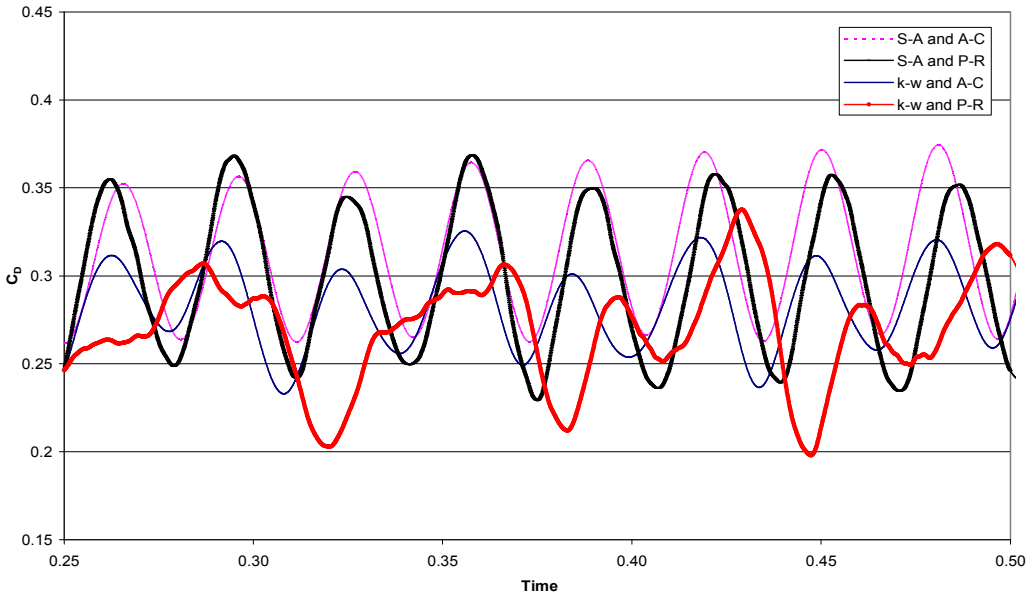

Figure 5.7 Drag coefficient vs. time for the middle-cylinder in the three-cylinder configuration.

Figure 5.8 shows that the magnitudes of C_L are very similar for all of the formulations. The oscillations of the periods of C_L for the artificial compressibility

algorithm appear to be constant. The period increases over the time history when the Preconditioned Roe algorithm is used. The preconditioned Roe algorithm has a smaller frequency than the artificial compressibility algorithm. The periods of oscillations are the same when the low-speed algorithms are the same. When the same turbulence model is used with different algorithms, the frequency of oscillations and the peak magnitudes do not correlate.

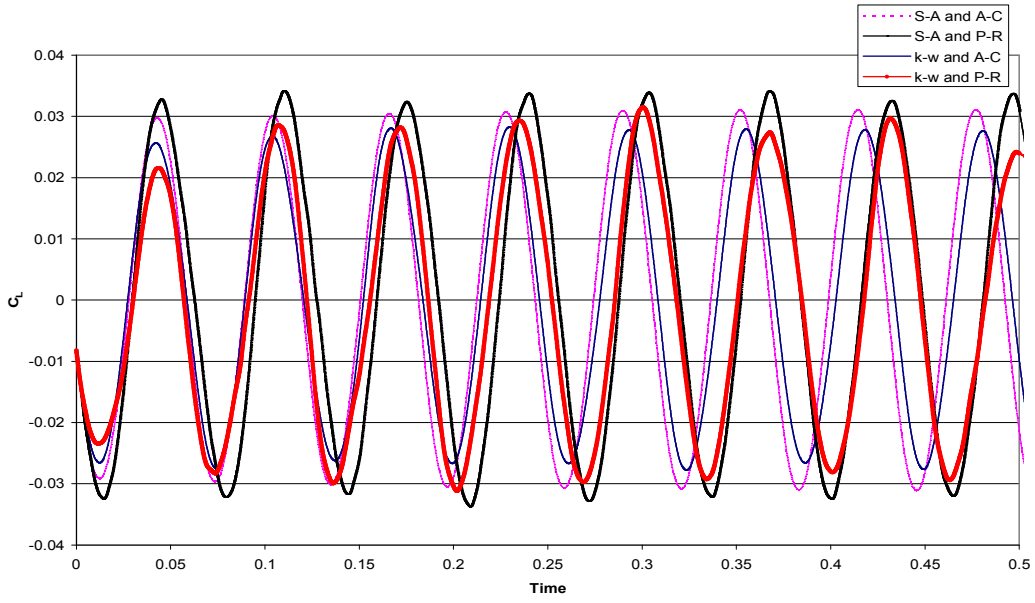

Figure 5.8 Lift coefficient vs. time for the middle-cylinder in the three-cylinder configuration.

The mean C_D and C_L predictions for the outer cylinder can be found in Table 5.5. The mean C_D values for all of the formulations are within 3% of each other. These values differ slightly from one another, but no trend with either turbulence model or low-speed algorithm is evident. The outer cylinders have less drag than the middle cylinder. The average C_D predicted of all of the cases for the middle cylinder was 0.28 compared to

0.25 for the outer cylinders. Less drag on the outer cylinders could be a result of the larger gap around the outer cylinders. The distance between the middle cylinder and the outer cylinders is smaller (1 diameter) than the distance between the outer cylinders and the walls (2.5 diameters). Also, the middle cylinder experiences the oscillations of the wakes of both the outer cylinders.

Table 5.5 Mean C_D and C_L for the outer cylinders in the three-cylinder configuration.

Formulation	Mean C_D	Mean C_L
Wilcox k-ω		
Artificial Compressibility	0.247	-0.0003
Preconditioned Roe	0.241	-0.0005
Spalart-Allmaras		
Artificial Compressibility	0.244	-0.0001
Preconditioned Roe	0.248	0.0003

A time history of the forces for the outer cylinders can be found in Figures 5.9 and 5.10. The drag coefficient is irregular with varying magnitudes. The Wilcox k-ω model with the preconditioned Roe algorithm prediction has the largest variations in magnitude and is non-sinusoidal, which is consistent with the middle cylinder predictions. The predictions from the two algorithms used with the Wilcox k-ω model do not correlate. However, when the algorithms are run in combination with the Spalart-Allmaras model, they have similar frequencies even though the patterns of both are irregular.

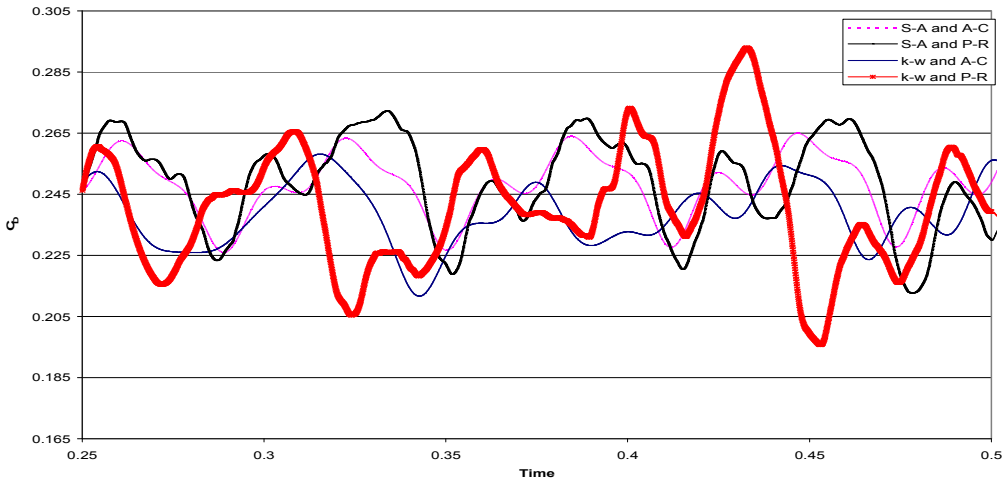

Figure 5.9 Drag coefficient vs. time for the outer-cylinders in the three-cylinder configuration.

A time history of the mean C_L of the outer cylinders is shown in Figure 5.10. The cylinders do not produce a net lift because they are not angled with respect to the flow. The conclusions that can be drawn from Figure 5.10 involve the frequencies of oscillations and the magnitudes of the C_L predictions. All four formulations begin at similar frequencies, but over time the preconditioned Roe algorithm shortens the frequency and changes the height of each peak. Figure 5.8 for the middle cylinder shows the same trend. The artificial compressibility algorithm predicts the same frequency and slightly different peak magnitudes for both turbulence models. The frequencies and peak magnitudes for the preconditioned Roe algorithm become more dissimilar with time.

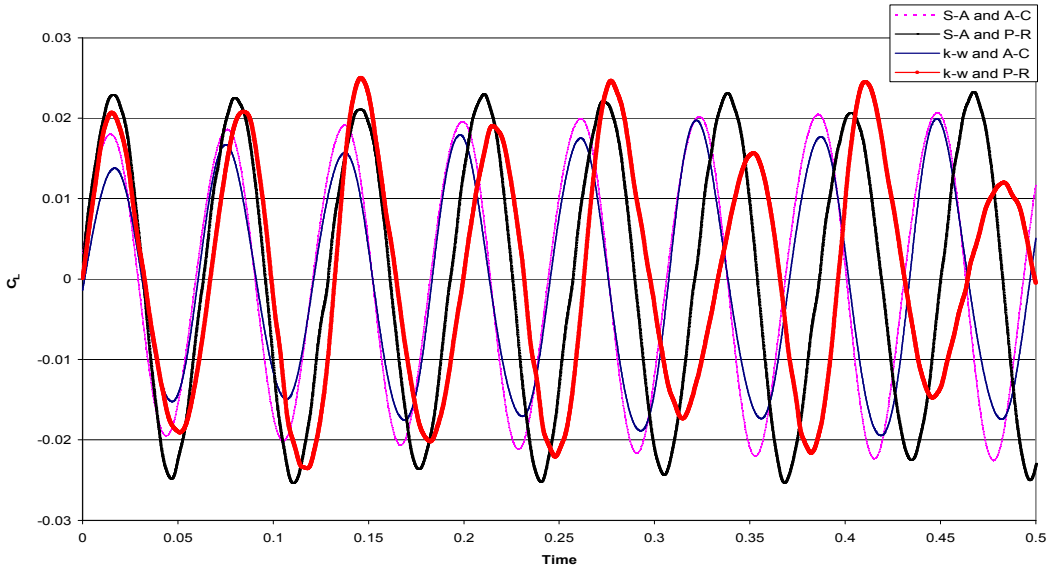

Figure 5.10 Lift coefficient vs. time for the outer-cylinders in the three-cylinder configuration.

The same trends were predicted for the outer and middle cylinders. The Spalart-Allmaras model was more consistent than the Wilcox k-ω model for drag prediction. The mean C_D of the middle cylinder was better predicted by the Spalart-Allmaras model. The lift force predictions were more sensitive to a change in turbulence model than a change in low-speed algorithm. The time histories of the force predictions were consistent if the artificial compressibility algorithm was used. The preconditioned Roe algorithm predicted more dissimilar behavior between the turbulence models. Over time, the preconditioned Roe algorithm reduced the frequency of oscillations for the lift coefficient.

5.3.3 Strouhal Number

The Strouhal number was calculated using Equation 5.1. Table 5.6 lists the St predictions for the middle cylinder. No experimental data was available for this configuration; as a result, the predictions will be compared with one another and loosely compared to the single-cylinder configuration results.

The low-speed algorithms used with either turbulence model produce approximately the same St for the middle cylinder. This is consistent with the force data found in Figures 5.7-5.10. The St predicted by the artificial compressibility algorithm was larger than predicted by the preconditioned Roe algorithm. Overall, the St did not differ more than 5% between the cases.

Table 5.6 Strouhal number for the middle-cylinder in the three-cylinder configuration

	St
Wilcox k-ω	
Artificial Compressibility	0.3086
Preconditioned Roe	0.2934
Spalart-Allamars	
Artificial Compressibility	0.3112
Preconditioned Roe	0.2972

Table 5.7 lists the St predictions for the outer cylinders. The difference in St for the formulations was less than 2%. The Wilcox k-ω model predicted slightly higher St than the Spalart-Almaras model. The St for the middle and outer cylinders was predicted by both algorithms and both turbulence models within 5% of each other.

Table 5.7 Strouhal number for the outer-cylinders in the three-cylinder configuration

Algorithm	St
Wilcox k-ω	
Artificial Compressibility	0.1575
Preconditioned Roe	0.1588
Spalart-Allamars	
Artificial Compressibility	0.1562
Preconditioned Roe	0.1549

The St for the outer cylinders agrees more closely with the St for the single-cylinder configuration than the middle cylinder. The larger gap spacing more closely resembles the unconfined boundary of the single-cylinder because the effect of the wall decreases with distance. The wake produced by the middle cylinder is compressed, which results in a higher shedding frequency and larger St. The shedding frequency of the middle cylinder is twice as large as the frequencies of the outer cylinders and the single-cylinder. The wall effects are present for the outer cylinders which results in a higher St for the outer cylinders than the single cylinder configuration.

5.3.4 Mean Velocity Magnitude

The predicted mean velocity variation across the duct 0.5 m downstream of the cylinders is compared to experimental data in Figure 5.11. The numerical data was averaged over the several cycles for each case. The experimental data (Nix[14]) was recorded over part of the duct height. The mean velocity magnitude of the experiment is constant at 19 m/s. The CFD data is given from top wall to bottom wall. The mean velocity magnitude across the test section for the Wilcox k-ω model was approximately

22 m/s, which is lower than the 23.5 m/s predicted with the Spalart-Allmaras model. All of the formulations over-predict the experimental velocity. The mean velocity for the Spalart-Allmaras model is 20% higher than experimental data whereas the Wilcox k-ω model is 17% higher. Looking at only the Wilcox k-ω model results, the mean velocity using the artificial compressibility algorithm is symmetric and fairly constant around 21 – 22 m/s. The preconditioned Roe algorithm predicts a dip at a normalized location 0.35 and is asymmetric across the test section. If an average of both algorithms is taken, it is approximately the same 22 m/s as stated above, but, the preconditioned Roe algorithm has a larger variance in magnitude than the artificial compressibility algorithm.

When used with the Spalart-Allmaras model, both algorithms predict large peaks in the center of the test section. The artificial compressibility algorithm predicts a peak 4 m/s larger than the preconditioned Roe algorithm. The preconditioned Roe algorithm has lower dips at 0.27 and 0.70 of the normalized height. The velocity at the dip corresponds to the experimental data but the remaining portion of the velocity does not correlate with the experiment or the other algorithm. The Spalart-Allmaras model has results that are symmetric.

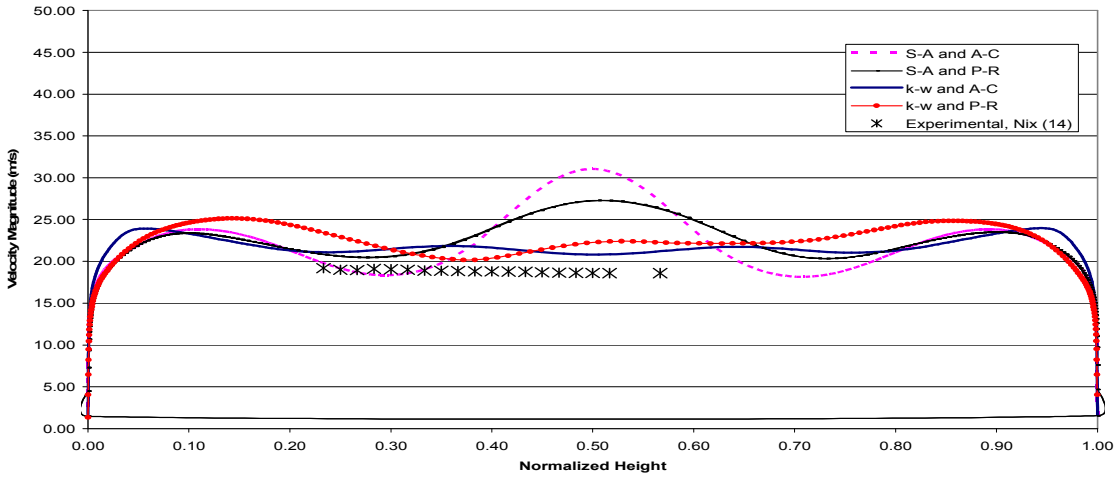

Figure 5.11 Velocity magnitude vs. normalized height 0.5 m downstream of cylinders for the three-cylinder configuration

In summary, both turbulence models, with either algorithm, over-predict the experiment. If the same turbulence model is used regardless of the low speed algorithm, similar predictions are achieved. The large variance in velocity behavior could be a result of 2D modeling of a 3D phenomenon. The eddies that are shed from the cylinders rotate and change in three dimensions experimentally, but the present computation only allows movement in the X-Y plane.

5.3.5 Turbulence Data

Results for the turbulence intensity and the ratio of eddy viscosity to laminar viscosity are discussed in this section. All data is recorded 0.5 m downstream of the cylinders and extends vertically from bottom wall to top wall. The turbulence intensity predictions are compared to experimental data.

The turbulence intensity predictions were calculated from Equation 5.2, and a comparison to the experiment can be found in Figure 5.12. The turbulence intensity is calculated from the turbulent kinetic energy, k. The k is directly output from GASP when the Wilcox k-ω model is used. There is no direct way to output the k when using the Spalart-Allmaras model. Therefore, only the Wilcox k-ω model predictions are compared to experimental data.

Both algorithms predict approximately the same behavior and values of turbulence intensity. The experimental data is steady at 10.4%. The peak value for both algorithms is 12%, but if the turbulence intensity is averaged across the height, it is 10% for both. The preconditioned Roe algorithm begins to dip at 0.5 of the normalized height, whereas the artificial compressibility algorithm does not. Both algorithms asymmetrically dip in the near-wall region. Since the experimental data was not taken near the wall, conclusions cannot be made on the accuracy of the predictions of the algorithms there. The algorithms do over-predict the experimental data, but the discrepancy is not large

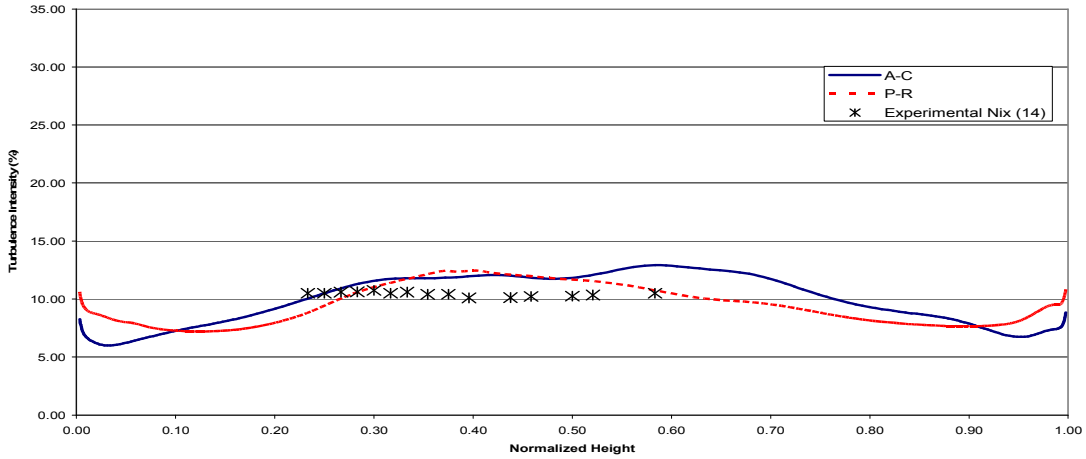

Figure 5.12 Turbulence intensity vs. non-dimensional time 0.5m downstream of cylinders for the three-cylinder configuration.

The eddy viscosity to laminar viscosity ratio is plotted in Figure 5.13. No experimental data was available for comparison. The ratio offers insight into the turbulence behavior of each formulation. The ratio predicted was similar for all four cases, predicting a maximum ratio of 400-450 in the center of the vertical plane. The Spalart-Allmaras model with the preconditioned Roe algorithm predicts a peak in the center of the vertical plane that is not predicted by the other cases. The Wilcox k-ω model predicts more turbulence near the wall. All four formulations predict very similar turbulence producing behavior.

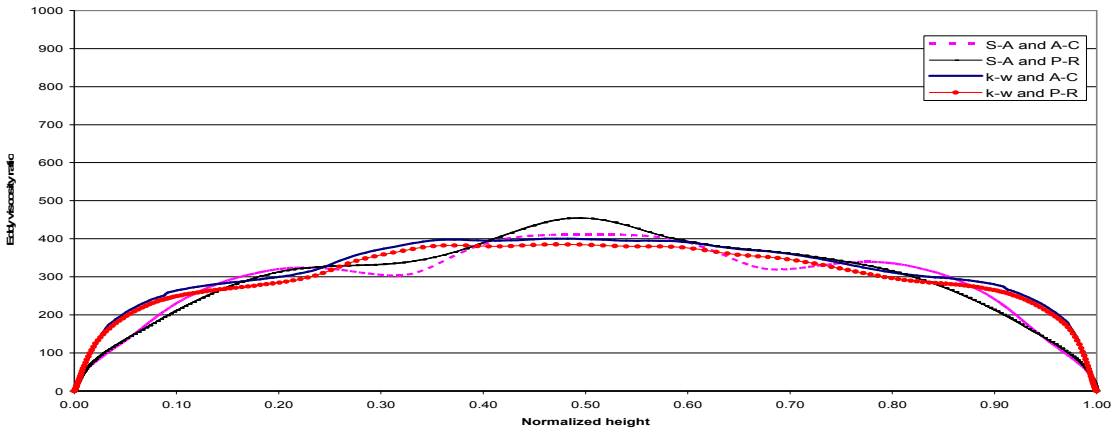

Figure 5.13 Eddy viscosity/laminar viscosity ratio vs. non-dimensional time 0.5m downstream of cylinders for the three-cylinder configuration.

5.3.6 Convergence Studies

In an effort to achieve a reasonable agreement between the formulations, two studies were performed, an inner cycle convergence study and a study of the influence of the compressibility parameter, β. As a "rule of thumb" a good value for β is $5*V^2$ where

V is the free-stream velocity. Three values for β were tested, $\beta = 5^* V^2$, $\beta = 10^* V^2$ and $\beta = 100^* V^2$. The results can be found in Figure 5.14. All three cases predicted similar trends, although the second and third cases were nearly identical. The first case had a small peak at the normalized duct location of 0.45. As a result of this plot, the predictions for the second case, $\beta = 10^* V^2$, were used for the three-cylinder configuration and for the single-cylinder configuration as well.

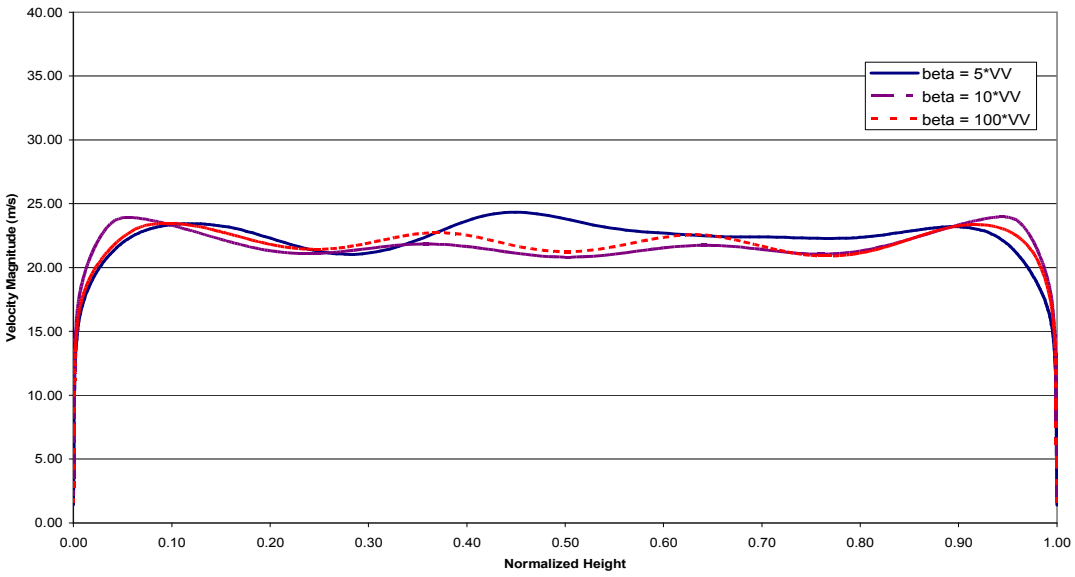

Figure 5.14 Beta comparison plot for the three-cylinder configuration.

The number of inner cycles per physical time step was varied between 5 and 10. Since there was not a large difference in the C_D predictions between 5 and 10 inner cycles, the number of inner cycles was not increased further. The results are shown in Table 5.7. As with the single-cylinder configuration, only the algorithms were studied. The Wilcox k-ω model was used for all of the cases. The C_D predictions were very

similar for 5 and 10 inner cycles. Therefore, 5 inner cycles was used for the predictions of the three-cylinder configuration.

Table 5.8 Inner cycle study for the three-cylinder configuration

Inner Cycles	C_D
Artificial Compressibility	
5	0.2834
10	0.2837
Preconditioned Roe	
5	0.2690
10	0.2684

Chapter 6: Summary and Conclusions

CFD results for unsteady, turbulent, low-speed flow around square cylinders with varying formulations is presented. Flow predictions from two different low-speed algorithms as well as two turbulence models were compared. The flow algorithms studied consisted of the artificial compressibility method applied to the incompressible RANS and a preconditioned Roe scheme for the compressible RANS. Both algorithms are shown to be viable options for solving low-speed, unsteady flows using a dual-time stepping procedure. The turbulence models used in this study were the one-equation Spalart-Allmaras model and the two-equation k-ω model by Wilcox.

The first configuration studied consisted of flow over a single square cylinder. Drag force and Strouhal numbers were compared to experimental data, and these comparisons showed that better correlations resulted from using the Spalart-Allmaras model. Varying the flow algorithm had much less impact on the solution than the turbulence model. Lift force history from the turbulence models consisted of sinusoidal like oscillations. While the solution from the Spalart-Allmaras model had a dominant, primary harmonic prediction, the solution from the k-ω model contained multiple frequencies with varying magnitudes. The convergence behavior of both flow algorithms was nearly the same.

The second configuration studied was a flow problem consisting of three, vertical, square cylinders spanning a duct. This case was modeled after an experiment in which mean velocity and turbulence intensity profiles were available. All of the formulations

over-predict the experimental mean velocity by 17 – 20%, but the k-ω model predicted a mean velocity profile closer to the experimental data by 3%. The largest velocity difference from experiment was found using the artificial compressibility algorithm and the Spalart-Allmaras model. This is the only occurrence in this research where the Wilcox k-ω model was more accurate, although, both models poorly predicted the velocity profile. The turbulence intensity was only compared for the k-ω model. Both algorithms predicted similar turbulence intensity behavior, slightly over-predicting the experiment. The four cases demonstrated similar aerodynamic force behavior to the single-cylinder configuration. The algorithm predictions of aerodynamic drag for both the middle and outer cylinders did not vary when the Spalart-Allmaras model was used, unlike when using the Wilcox k-ω model. Better correlation between low-speed algorithms for the lift coefficient was obtained with artificial compressibility.

The numerical Strouhal number of all four cases for the middle and outer cylinders did not vary more than 5%. The middle-cylinder produced a frequency that resulted in a Strouhal value twice as large as the outer cylinders. The three-cylinder configuration was confined by the tunnel walls which had the effect of increasing the shedding frequencies of the cylinders when compared to the unconfined single-cylinder configuration. Like the single cylinder computations, both flow algorithms had very similar convergence behavior when run using the dual-time stepping procedure.

In summary, the following main conclusions can be made:

- The predictions are more sensitive to the turbulence model choice than to the choice of algorithm.
- Both low-speed algorithms adequately predicted the flow behavior.

- If the turbulence model was changed, less variation in the predictions was found when using the artificial compressibility algorithm over the preconditioned Roe algorithm.
- The Spalart-Allmaras model overall produced better results with both algorithms than the Wilcox k-ω model.
- Confining the cylinders increased the shedding frequency.

The CFD simulations performed here were done using two-dimensional simulations. Future research should be done involving three-dimensional computations, which will better represent the physics of three-dimensional vortex shedding and vortex behavior.

Chapter 7: References

[1]Patankar, S.V., *Numerical Heat Transfer and Fluid Flow*, McGraw-Hill, New York, 1980.

[2]Issa, R. I., "Solution of the Implicitly Discretized Fluid Flow Equations by Operator-Splitting" *Journal of Computational Physics*, Vol 62, pages 40-65, 1985

[3]Patankar, S. V., *Numerical Heat Transfer and Fluid Flow Hemisphere*, Washington D.C. 1980

[4]Rogers, S.E. and Kwak, D., "An Upwind Differencing Scheme for Time-Accurate Incompressible Navier-Stokes Equations," *AIAA Journal*, Vol. 28, 1990, pp.253-262

[5]Chorin, A.J., "A Numerical Method for Solving Incompressible Viscous Flow Problems," *Journal of Computational Physics*, Vol. 2, No. 1, 1967, pp. 12-26.

[6]Weiss, J.M. and Smith, W. A., "Preconditioning Applied to Variable and Constant Density Flows," *AIAA Journal*, Vol. 33, No. 11, 1995, pp.2050-2057.

[7]R. Neel, A. Godfrey, and W. McGrory, "Low-Speed, Time-Accurate Validation of GASP Version 4"AIAA 2005-0686

[8]Wilcox, D. C., *Turbulence Modeling for CFD*, DCW Industries, 1st ed., 1998

[9]Pope, Stephen B., *Turbulent Flows*, Cambridge University Press, 2000.

[10]Lo, S.C., Hoffmann, K.A. and Dietiker, J.F., "Numerical Investigation of High Reynolds Number Flows Over Square and Circular Cylinders." *Journal of Thermophysics and Heat Transfer,* 19, 2005, pp. 72-80.

[11]Spalart, P.R. and Allmaras, S.R., "A One Equation Turbulence Model for Aerodynamic Flows," AIAA Paper 78-257, 1994.

[12]Gridgen Version 13.3 user Manual, Pointwise, Inc., PO Box 210698, Bedford, TX 76095. 1999

[13]Lee, B.E., "The Effect of Turbulence on the Surface Pressure Field of a Square Prism." *Journal of Fluid Mechanics*, 69, 1975, pp. 263-282.

[14]. Norberg, "Flow Around Rectangular Cylinders: Pressure Forces and Wake Frequncies," *J. Wind Eng. Ind. Aerodynamics*, 8, 1981, pp. 211-222 and 19, 1993, pp. 187- 196.

[15]Vanleer, B. “Towards the Ultimate Conservative Difference Scheme. IV. A Second Order Sequel to Godunov’s Method,” *Journal of Computational Physics*, Vol. 32, pp. 101-136.

[16]Nix, A.C., Smith, A.C., Diller, T.E., Ng, W.F., Thole, K.A., “High Intensity Large Length-Scale Freestream Turbulence Generation in a Transonic Cascade Tunnel.” ASME 2001

[17]Sayers, A.T. “Steady-State Pressure and Force Coefficients for Groups of Three Equispaced Square Cylinders Situated in a Cross Flow.” *J. Wind Eng. Ind. Aerodynamics*, 37, 1991, pp. 197-208.

[18]Tannehill, John C., *Computational Fluid Mechanics and Heat Transfer 2nd ed*., Taylor and Francis, 1997

[19]Kwak, Dochan and Kiris, Cetin, “Success and Challenges of Incompressible Flow Simulation.” AIAA 2003-3440.

[20]Venkateswaran, S., Buelow, P.E.O. and Merkle, C.L., “Development of Linearized Preconditioning Methods for Enhancing Robustness and Efficiency of Euler and Navier-Stokes Computations.” AIAA 97-2030.

[21]Hortsman, C.C., Kussoy, M.I. and Lanfranco, M.J., “An Evaluation of Several Compressible Turbulent Boundary –Layer Models: Effects of Pressure Gradient and Reynolds Number.” AIAA 78-1160.

[22]Wilcox, David C., “A Half Century Historical Review of the k-ω Model.” AIAA 91-0615

[23]Rodi, W., “Comparison of LES and RANS Calculations of the Flow Around Bluff Bodies.” *J. Wind Eng. Ind. Aerodynamics,* 69-71, 1997, pp. 55-75.

[24]Lee, Sangsan, “Unsteady Aerodynamic Force Prediction on a Square Cylinder using k-ε Turbulence Models.” . *Wind Eng. Ind. Aerodynamics,* 67 & 68, 1997, pp. 79-90

[25]Murakami, S., Mochida, A., “On Turbulent Vortex Shedding Flow Past 2D Square Cylinder Predicted by CFD” *J. Wind Eng. Ind. Aerodynamics,* 54 & 55, 1995, pp. 191-211.

[26]Krajnovic, S. and Davidson, L., “Large Eddy Simulation of the Flow Around a Three-Dimensional Bluff Body.” AIAA 2001-0432.

[27]Taylor, Ian and Vezza, Marco, “Prediction of Unsteady Flow Around Square and Rectangular Section Cylinders Using Descrete Vortex Method,” *J. Wind Eng. Ind. Aerodynamics*, No. 82, 1999, pp. 247-269.

[28]Tamura, Testuro, "Numerical Study of Aerodynamic Behavior of a Square Cylinder." *J. Wind Eng. Ind. Aerodynamics*, 33, 1990, pp. 161-170.

[29]Rogers, S.E., Kwak, Dochan and Kiris, Cetin, "Steady and Unsteady Solutions of the Incompressible Navier-Stokes Equations." *AIAA Journal*, 29, April 1991

[30]GASP Version 4 Technical Reference, AeroSoft Inc. Blacksburg, VA

[31]Neel, R.E., Godfrey, A.G. and Slack, D.C., "Turbulence Model Validation in GASP Version 4" AIAA paper 2003-3740, 2003.

[32]Sohankar, Ahmad and Davidson, L., "Large Eddy Simulation of Flow Past a Square Cylinder: Comparison of Different Subgrid Scale Models," *Journal of Fluids Engineering*, Vol. 122, 2000, pp. 39-47.

[33]Lyn, D. A., Elnav, S., Rodi, W., and Park, J.H., "A Laser Doppler Velocimetry Study of the Ensemble-Averaged Characteristics of the Turbulent Near Wake of a Square Cylinder," *Journal of Fluid Mechanics*, Vol. 304, 1995, pp. 285-319.

[34]Blevins, Robert D., *Flow-Induced Vibration*, Van Nostrand Reinhold, 2nd ed., 1990.

[35]Seror, S., Rubin, Theodor and Peigin, S., "Implementation and Validation of the Spalart–Allmaras Turbulence Model in Parallel Environment" *Journal of Aircraft*, 42, 2005.

[36]Ghee,Terence A., and Keyser David R., "Basic Aerodynamic Shapes in a Low-Speed, Highly Turbulent Flow." AIAA 2003-3953

[37]Bradshaw, P., Launder, B.E. and Lumley, J.L., "Collaborative Testing of Turbulence Models." AIAA 91-0215.

[38]Coakley, T.J., "Turbulence Modeling Methods for Compressible Navier-Stokes Eqautions." AIAA 83-1693

[39]Lakehal, D., Rodi, W., "Calculation of the Flow Past a Surface-Mounted Cube with Two-Layer Turbulence Models." *J. Wind Eng. Ind. Aerodynamics,* 67 & 68, 1997, pp. 65-78.

[40]Wong, P.T.Y., Ko, N.W.M., Chiu, A.Y.W., " Flow Characteristics Around Two Parallel Adjacent Square Cylinders of Different Sizes." *J. Wind Eng. Ind. Aerodynamics,* 54 & 55, 1995, 263-275

[41]Menter, F.R., "Two-Equation Eddy-Viscosity Turbulence Models for Engineering Applications." *AIAA Journal*, 32, 1994, pp.1598-1605

[42]Rubesin, Morris W., “Turbulence Modeling for Aerodynamic Flows.” AIAA 89-0606

Vita

Theresa Lynn Campioli was born January 16, 1981 in Fairfax, VA, daughter of Carl M. Campioli and Carolyn L. Campioli. She has two sisters, Jennifer Cannan (28) and Mary Campioli (22). Theresa attended Bishop Denis J. O'Connell High School in Arlington, VA, graduating in 1999. Theresa went on to attend Auburn University and received a Bachelors of Science degree in Aerospace Engineering in May 2003. During her time at Auburn she was a member of the NCAA division I soccer team. In fall of 2003, Theresa began her graduate education at Virginia Polytechnic Institute and State University working for Dr. Joseph Schetz. Upon the completion of this thesis in May 2005, Theresa will receive a Masters of Science degree in Aerospace Engineering. She has plans to continue her formal education by pursing a Doctor of Philosophy degree through VA Tech in conjunction with Aerojet. She will also begin working for Aerojet in the summer of 2005.